The uptake of small extracellular vesicles by recipient cells is facilitated by paracrine adhesion signaling

Koichiro M. Hirosawa[1], Yusuke Sato[2], Rinshi S. Kasai[3], Eriko Yamaguchi[1], Naoko Komura[1], Hiromune Ando[1,6], Ayuko Hoshino[4], Yasunari Yokota[5], Kenichi G. N. Suzuki[1,3,6]*

[1]Institute for Glyco-core Research (iGCORE), Gifu University, Gifu, 501-1193, Japan

[2]Department of Chemistry, Graduate School of Science, Tohoku University, Sendai, 980-8578, Japan

[3]Division of Advanced Bioimaging, National Cancer Center Research Institute (NCCRI), Tokyo, 104-0045, Japan

[4]Research Center for Advanced Science and Technology, University of Tokyo, Tokyo, 153-8904, Japan

[5]Department of Electrical, Electronics and Computer Engineering, Faculty of Engineering, Gifu University, Gifu, 501-1193, Japan

[6]Institute for Integrated Cell-Material Sciences, Kyoto University, Kyoto, 606-8501, Japan

***Corresponding author**

Kenichi G.N. Suzuki, E-mail: suzuki.kenichi.b7@f.gifu-u.ac.jp

Abstract

Small extracellular vesicles (sEVs) play critical roles in intercellular communication. However, the mechanisms by which sEVs are internalized by recipient cells remain unclear. Here, we investigated these mechanisms through state-of-the-art imaging techniques. Single-molecule imaging revealed that tumor-derived sEVs can be divided into several subtypes. By simultaneously performing single sEV-particle tracking and super-resolution movie observation of membrane invaginations in living cells, we discovered that all sEV subtypes were internalized via phagocytosis, while some subtypes that recruited raft markers were endocytosed via caveolae. Furthermore, we demonstrated that integrin β1 and talin-1 accumulated in recipient cell plasma membranes underneath all sEV subtypes. Paracrine, but not autocrine, sEV binding triggers Ca^{2+} mobilization, which is induced by the activation of Src family kinases and PLCγ. Ca^{2+}-induced activation of calcineurin-dynamin subsequently promoted sEV internalization, leading to the recycling pathway. Thus, we elucidated the detailed mechanisms of sEV internalization, which is facilitated by paracrine adhesion signaling.

Extracellular vesicles (EVs) are secreted by most cells into the surrounding environment. For more than a decade, small EVs (sEVs), also called exosomes, have gained extensive attention as pivotal mediators of intercellular communication; sEVs can transfer bioactive molecules, such as proteins, lipids, and nucleic acids to recipient cells, altering their physiology and function[1]. Despite their importance, the mechanisms by which sEVs are internalized by recipient cells are poorly understood. Several studies have suggested that sEV uptake is complex and heterogeneous and can occur through various mechanisms, such as direct fusion between sEVs and recipient cell plasma membranes (PMs), endocytosis, and phagocytosis[2]. However, the specific pathways and factors that determine sEV uptake remain unknown. Furthermore, since not all EVs are created equally and different subtypes of EVs have distinct functions and compositions[3–6], the behaviors of individual sEV subtypes should be investigated. The uptake mechanisms may vary depending on the subtype of sEVs or recipient cells, but this possibility has not been investigated[7]. Clarifying the uptake mechanisms of sEVs is critical for developing effective strategies for sEV-based therapies and diagnostics[8,9]. Moreover, elucidating the factors that regulate sEV uptake would provide insights into the biological functions of sEVs and their roles in various physiological and pathological processes[10].

In this study, we initially examined whether sEVs derived from two distinct tumor cell lines can be divided into discrete subtypes by employing single-particle imaging with single-molecule detection sensitivity. In addition, to elucidate the mechanisms involved in sEV uptake by recipient cells, we sought to assess the colocalization of sEVs with membrane invaginations

or signaling molecules in living cell PMs at high temporal and spatial resolutions. For this purpose, we developed cutting-edge techniques, which allowed us to capture super-resolution photoactivated localization microscopy (PALM) movies in a pseudo-real-time manner, as opposed to static images. Furthermore, we performed simultaneous dual-color observations of individual sEV particles and super-resolution 3D images of intracellular membrane structures.

Results

Validation of the presence of small extracellular vesicle (sEV) subtypes

Several studies have suggested that sEVs, even when released from a single cell type, exhibit a biased molecular composition, and it is plausible that subtypes of sEVs may exist[3,11,12]. Therefore, as a starting point for analyzing the interaction of sEVs with their recipient cells, we sought to verify the presence of sEV subtypes originating from two distinct tumor cell lines. When two fluorescently labeled antibodies are used simultaneously to label two sEV marker proteins, which is the most frequently used method, each antibody may prevent the other antibody from binding to the marker proteins[6]. In addition, since the number of dye molecules per antibody molecule follows a Poisson distribution and the dye/antibody ratio is not always 1, we cannot determine the presence or absence of marker proteins in an sEV particle. Therefore, to overcome this problem in validation of the presence of sEV subtypes, we used sEVs containing tetraspanin marker proteins, such as CD63, CD9 and CD81 fused with monomeric GFP (mGFP)

or Halo7-tag labeled with TMR at very high efficiency (Extended Data Fig. 1a). Under this condition, the marker proteins are labeled with fluorophores at the dye/protein ratio of 1. Then, individual particles of sEVs were visualized by total internal reflection fluorescence microscopy (TIRFM) with single-molecule detection sensitivity (Fig. 1a and Extended Data Fig. 1b).

For this purpose, we expressed both mGFP-tagged and Halo7-tagged marker proteins in donor cells and collected sEVs from the cell culture medium. To ascertain the presence or absence of marker proteins in sEVs, it was necessary to isolate stable cell lines that express both mGFP and Halo7-tagged marker proteins, but do not overexpress them to avoid detrimental effects. First, the stable cell lines were isolated by a cell sorter (Fig. 1b), and Western blotting analysis was performed with the obtained sEVs (Fig. 1c). The results revealed that the copy numbers of all three (CD63, CD9, and CD81) exogenous tetraspanin marker proteins tagged with mGFP or Halo7 were 0.1-0.5 times smaller than those of the endogenous proteins. By fitting the histograms of the fluorescence intensities of tetraspanins-Halo7-TMR with lognormal function curves (Online Methods), the numbers of tetraspanins-Halo7 per sEV were estimated to be 4.2-4.8 (Fig. 1d and Extended Data Fig. 1b and c). Assuming that the numbers in each sEV particle follow a Poisson distribution, 98.5% to 99.2% of sEVs should contain at least one labeled tetraspanin molecule, indicating that nearly all sEVs were detected. Furthermore, since the amounts of the tetraspanin-mGFP were similar to those of the tetraspanin-Halo7 (Fig. 1b and c), almost all sEVs should contain the tetraspanin-mGFP. According to simultaneous two-color observations of sEVs, a large fraction of the sEVs contained both CD9-mGFP and CD9-Halo7-

TMR, which were used as positive controls. Meanwhile, only a small fraction of the sEVs contained both CD9-mGFP and CD63-Halo7-TMR (Fig. 1e). A similar analysis of all combinations of tetraspanin marker proteins is shown in Fig. 1f. As illustrated in the Venn diagram, two subtypes of sEVs are derived from PC-3 cells, one containing only CD63 and the other containing all three marker proteins CD9, CD63 and CD81. In addition, two subtypes of sEVs are derived from 4175-LuT cells, one containing CD9 and CD63 and the other containing all three markers.

sEV subtypes exhibit similar diameters but different membrane packing

The physical properties of each subtype of sEVs were characterized. Transmission electron microscopy (TEM) images obtained by negative staining (Fig. 2a) revealed that the sEVs isolated by ultracentrifugation without subtype fractionation were 79 ± 18 nm (mean ± SD) in diameter, which was consistent with the value (71 ± 7 nm) measured by the electrical resistance nanopulse method (qNANO) (Fig. 2b). Subsequently, we performed super-resolution microscopy (dSTORM) to estimate the diameters of the sEV subtypes. Liposomes containing SaraFluor 650B-GM3 (SF650B-GM3) with a diameter of 111 ± 21 nm, as measured by the nanopulse method, were used as a reference standard. Segmentation of the super-resolution images from the localization coordinates of SF650B was executed employing a Voronoi diagram using SR-Tesseler[13], and the diameters of the sEV subtypes were estimated as described in the Methods section (Fig. 2b and c). By analyzing liposomes with more than 100 localizations of SF650B, we

accurately determined that the diameter of the liposomes was 110 ± 25 nm (Fig. 2b and Extended Data Fig. 2), which was highly consistent with that measured by the nanopulse method (Fig. 2b). The diameters of the sEVs, which included CD9-, CD63-, and CD81-Halo7 labeled with the SF650B-halo ligand, were determined to be 81 ± 24, 71 ± 22, and 71 ± 27 nm, respectively (Fig. 2b), indicating that the diameters of the different sEV subtypes are comparable.

To further characterize the sEV subtypes derived from PC-3 cells, the membrane packing of each sEV subtype was quantitatively analyzed using a probe (ApoC-TAMRA) that recognizes membrane defects[14]. The average fluorescence intensity was significantly lower for ApoC-TAMRA bound to sEVs containing CD63-mGFP than those bound to sEVs containing CD81-mGFP or CD9-mGFP, indicating that membrane packing was greater in sEVs containing CD63-mGFP (Fig. 2d). Furthermore, CD63-Halo7-containing sEVs isolated by Tim-4 affinity beads have a diameter similar to that of CD81-Halo7- or CD9-Halo7-containing sEVs (Extended Data Fig. 3a) but have greater membrane packing, as revealed by the fluorescence intensities of ApoC-TAMRA (Extended Data Fig. 3b) and another membrane defect-sensing probe, the TAMRA-conjugated amphipathic helix (peptide 2-23) of α-synuclein bound to the sEVs[15] (Extended Data Fig. 3c). Since membrane packing is closely correlated with membrane fluidity[16,17], the membrane fluidity of CD63-containing sEVs may be lower than that of CD9- and CD81-containing sEVs . In addition, these results explicitly demonstrate that the behaviors of sEVs must be investigated subtype by subtype.

Endocytosis of sEVs is controlled by the dynamin-related uptake machinery

Subsequently, we investigated the mechanism underlying the endocytosis of sEVs by recipient cells using new microscopic techniques (Fig. 3a). First, sEVs containing CD63-Halo7-SaraFluor650T (SF650T) (10^{11} particles/ml) were added to recipient PZ-HPV-7 cells (1.0×10^6 cells), and the dynamic behavior of the sEVs on the PM was observed using a 3D single fluorescent-molecule observation system with a cylindrical lens (Fig. 3a-c, Extended Data Fig. 4 and Supplementary Movie 1). The sEV particles moved linearly in the plane of the PM (Fig. 3b), while they were internalized by changing the z-coordinate at a rate of 20 nm/s with repeated fluctuations (Fig. 3c). Second, the uptake rates of each sEV subtype were assessed by confocal microscopy, and no significant difference among the subtypes was observed 20 min or longer after sEV addition (Fig. 3d). In addition, sEVs and fluorescent dextran were simultaneously observed and were found to strongly colocalize within 48 min after dextran addition (Fig. 3e). These results suggest that most sEVs are internalized by cells through endocytosis rather than through fusion with the PM. This result is supported by our single-molecule observation, which revealed that no mGFP-GPI molecules underwent lateral diffusion in the recipient cell PM even 120 min after sEVs including mGFP-GPI were attached to the PM (Fig. 3f). Importantly, sEV uptake was greatly decreased in cells overexpressing the dominant negative mutant of dynamin (Fig. 3g and h), indicating that dynamin-mediated endocytosis via clathrin-coated pits, caveolae and phagocytosis, etc.[7,18,19], plays a critical role in sEV uptake.

Routes of sEV endocytosis in recipient cells are dependent on sEV subtypes

We sought to determine the methods by which tumor PC-3 and 4175-LuT cell-derived sEVs are transported into normal recipient PZ-HPV-7 and WI-38 cells, respectively, through membrane invagination. Since PC-3 and PZ-HPV-7 cells are human epithelial prostate cancer and normal cells, respectively, we considered the combination as a model of sEV transfer between neighboring cells in the same tissue. Meanwhile, it has been known that sEVs derived from 4175-LuT human breast cancer cells preferentially bind to WI-38 normal human lung fibroblast cells, and the combination is considered a model of sEV-mediated organotropic metastasis[20]. For this purpose, we simultaneously observed single sEV particles and membrane invaginations (Fig. 4a and b). For PALM observation, mEOS4b-fused AP2α, caveolin-1 (CAV1), or LAMP2, which are marker proteins for clathrin-coated pits[21], caveolae[22], and phagocytic regions[23], respectively, were expressed in the recipient PZ-HPV-7 cells or WI-38 cells. We simultaneously performed PALM data acquisition by single-molecule observation of the mEOS4b spots at a high speed (5 ms/frame) and single-particle observation of sEVs labeled with SF650T. To obtain one PALM image, data acquisition was performed for 1002 frames, which was then repeated by shifting the initial frames backward by 6 frames (30 ms); a total of 669 PALM images were obtained. By connecting these PALM image sequences, we generated a pseudo-real-time PALM movie (Fig. 4b). A parameter-free image resolution estimation method based on correlation analysis[24] revealed that the spatial resolution in each frame of the PALM movie is 21 ± 0.4 nm (Extended Data Fig. 5a and b). In living cell PMs, therefore, caveolae can be distinguished as two distinct

structures, which cannot be resolved by conventional methods (Extended Data Fig. 5a). Furthermore, the PALM image sequence acquired every 5 seconds showed that caveolae were forming and disappearing on this timescale (Extended Data Fig. 5a), indicating that PALM movies should be generated to follow changes in membrane invagination. Images of single sEV particles were simultaneously recorded at 5 ms/frame, and the average images for 6 frames were connected to create the movie. Pseudo-real-time movies of membrane invaginations and single particles of sEVs were superimposed.

We found that PC-3-derived sEV particles containing CD63-Halo7-SF650T frequently colocalized with caveolae and phagocytic regions in the PZ-HPV-7 cell PM (Fig. 4c-e and Supplementary Movies 2 and 3). We further quantitatively analyzed the colocalization of these proteins (Fig. 5a). The contours of the membrane invaginations in PALM images were defined by binarization using kernel density estimation (KDE), which is the most useful method for analyzing protein clusters[25,26]. Subsequently, the distance from the contour to the center of the sEVs on the PM was measured, and the number densities of pairwise distances at a given distance were plotted. The number densities at each distance were normalized to those of randomly generated points in silico; therefore, y-axis values greater than 1 in the negative x-axis region (color-highlighted area in Fig. 5b) indicate that sEV particles are enriched within the membrane invagination. Fig. 5b and c show that none of the sEV subtypes derived from PC-3 or 4175-LuT cells were concentrated in the AP2α-labeled clathrin-coated pits of the recipient PZ-HPV-7 or WI-38 cells, respectively. In contrast, all sEV subtypes derived from both cell lines

were enriched in LAMP2-labeled phagocytic regions in both types of recipient cells. Interestingly, only the CD63-Halo7-containing sEV subtype derived from PC-3 cells colocalized with CAV1-labeled caveolae on the recipient PZ-HPV-7 cells (Fig. 4c, middle; Fig. 5b and c, top-middle). Furthermore, sEVs containing CD81-Halo7-SF650T, namely the sEV subtype containing all three marker proteins derived from 4175-LuT cells (shaded circles in the Venn diagram in Fig. 1f) were also enriched in caveolae on the recipient WI-38 cells (Fig. 5b and c bottom-middle). The results shown in Figs. 1f, 4c, 5b, and c indicate that the enrichment of sEVs in caveolae of the recipient cells is dependent on the sEV subtype. Furthermore, simultaneous two-color 3D super-resolution images of caveolae and PC-3-derived sEVs containing CD63-Halo7-SF650T revealed that the sEV particles colocalized with caveolae on the PZ-HPV-7 cell PM in a parallel and perpendicular manner to the PM (Fig. 5d).

Next, we investigated the fate of intracellular sEVs after they were internalized. sEVs may have colocalized with recycling endosomes, as suggested by two-color 2D simultaneous observation of single particles of sEVs and super-resolution dSTORM images of the recycling endosome marker mEOS4b-Rab11 (Fig. 5e, top). Furthermore, 3D observation (Fig. 5e, bottom) more explicitly and quantitatively showed that 20-40% of all the subtypes of sEVs were colocalized with recycling endosomes 3 to 6 h after the addition of sEVs to PZ-HPV7 cells (Fig. 5f), although whether EVs fused with recycled endosomal membranes was unclear. Since the number of fluorescently labeled Rab11 molecules per recycling endosome was estimated to be 17.6±3.7 according to a previously reported method[26], almost all recycling endosomes were

visualized. The degree by which the different sEV subtypes colocalized with the recycling endosome marker was indistinguishable (Fig. 5f). Our recent study revealed that integrin heterodimers in tumor cell-derived sEVs are specifically bound to laminin but scarcely bind to fibronectin on recipient cell PMs[27]. In agreement with these findings, researchers have reported that internalized integrin α6, a component of the laminin receptor (α6β1 and α6β4), in cells that adhere to laminin is readily transported to recycling endosomes; in contrast, integrin α5, a component of the fibronectin receptor (α5β1), is not transported[28]. These results, together with our recent work[27] suggest that 20-40% of the sEV particles bound to laminin on cell PMs were internalized and transported into the recycling pathway, either in the intact or membrane-fused form.

Binding of sEVs to the recipient cell PM induces an integrin-based signaling platform

Next, we sought to elucidate the molecular mechanisms responsible for the specific colocalization of sEVs containing CD63 derived from PC-3 cells with caveolae. To this end, we investigated whether molecular assemblies are formed in the PM of the recipient PZ-HPV-7 cell just underneath the sEV binding site to facilitate colocalization of the sEVs with caveolae. We conducted colocalization analysis by simultaneously observing single particles of sEV subtypes and single membrane molecules in the PM using a cross-correlation-based method (Extended Data Fig. 6). The lipid composition of caveolae is similar to that of lipid rafts[29], and GPI-anchored proteins, a representative raft marker, are concentrated in caveolae upon crosslinking[30].

Dual-color single-molecule imaging revealed that single Halo-GPI molecules were enriched only in the PM area underneath sEVs containing CD63-Halo7-SF650T but not in the PM area underneath sEVs containing CD81- or CD9-Halo7-SF650T (Fig. 6a and b and Supplementary Movie 4). These results suggest that the PM underneath CD63-sEVs exhibits a stronger affinity for raft markers than that underneath sEVs containing CD81 or CD9, leading to the enrichment of CD63-sEVs in caveolae.

Since caveolin-1-dependent endocytosis of integrin β1 has been reported[31], we sought to examine the recruitment of integrin β1 to the membrane underneath the different subtypes of sEVs. Our results revealed that integrin β1 was frequently recruited to and enriched in the PM underneath the sEVs of all the subtypes (Fig. 6a and b and Supplementary Movie 5). Moreover, simultaneous observation of PALM movies and single sEV particles revealed that talin-1, an inside-out signaling molecule that triggers integrin activation[32], was also enriched in the PM underneath sEVs containing CD63-Halo7-SF650T (Fig. 6c, Supplementary Movie 6). These results suggest that integrin β1 clusters are formed in the PM underneath sEVs, which induces cluster formation of talin-1, leading to the activation of integrin. Recently, we demonstrated that integrin heterodimers in all subtypes of sEVs containing CD63, CD81 or CD9 bind to laminin on recipient cell PMs[27]. Consequently, integrin β1, which is recruited to the PM underneath sEVs, likely interacts with laminin, suggesting that a symmetrical integrin structure forms through laminin between sEVs and the recipient cell PM (Fig. 6d). Importantly, this symmetrical structure appears to be consistent across all examined subtypes of sEVs.

Paracrine sEV binding triggers the Ca^{2+} response in recipient cells

Integrin clustering is known to trigger the recruitment of structural and signaling proteins, which leads to the formation of an adhesion complex[33,34]. This process triggers intracellular signaling, such as the intracellular Ca^{2+} response[35,36]. Therefore, we investigated whether intracellular signaling is induced by the accumulation of integrin underneath sEVs in the recipient cell PM. Initially, we monitored the change in the intracellular Ca^{2+} concentration using the Fluo-8H indicator after the addition of sEVs isolated by ultracentrifugation. As shown in Fig. 7a and b, Extended Data Fig. 7, and Supplementary Movie 7, the intracellular Ca^{2+} concentration transiently increased within a few minutes after the addition of sEVs (5.0×10^9 particles/ml at the final concentration that is lower than the concentration in human blood plasma[37]). We also discovered that the intracellular Ca^{2+} response was triggered by the addition of sEVs isolated from Tim-4 affinity beads but not by the addition of exomeres[38], which were isolated by treating the supernatant with Tim-4 beads after ultracentrifugation to completely remove the sEVs (Fig. 7c). Based on these results, the intracellular Ca^{2+} response is triggered by the binding of sEVs to the PM and not by contaminating factors. Furthermore, the immediate increase in intracellular concentration of Ca^{2+} after sEV was added indicates that sEV binding induced prompt signaling in the PM rather than a secondary response after sEV uptake[39,40].

Next, intracellular Ca^{2+} concentrations in recipient cells were quantified after sEVs derived from 3 kinds of donor cells were incubated with 3 kinds of recipient cells (9

combinations) (Fig. 7d). Remarkably when sEVs were added to the cells that secreted them, no intracellular Ca^{2+} response was detected (Fig. 7d) even though sEVs bound to the cell PMs (Extended Data Fig. 8a and b, open symbols). On the other hand, sEVs derived from two cancer cell lines, PC-3 and 4175-LuT, as well as primary mesenchymal stem cells (MSCs) bound to different recipient cell PMs and induced intracellular Ca^{2+} responses in the recipient cells (Fig. 7d). Furthermore, when sEVs did not bind to recipient cells, no Ca^{2+} response was observed (4175-LuT-derived sEVs vs. PZ recipient cells) (Fig. 7d and Extended Data Fig. 8). These results unequivocally show that an intracellular Ca^{2+} response is induced by the binding of paracrine sEV to recipient cells, whereas this response is not achieved by autocrine sEV binding.

To further verify whether the intracellular Ca^{2+} response is triggered by the adhesion signaling induced by sEVs on the PM, we examined the Ca^{2+} response in recipient cells overexpressing the dominant negative mutant of talin-1 (TalinDN). As shown in Fig. 7e, the intracellular Ca^{2+} response was notably suppressed, indicating that the adhesion signaling mediated by sEVs is responsible for inducing the Ca^{2+} response.

Since the Src family kinases, PLCγ and FAK have been reported to be involved in integrin adhesion signaling[36,41,42], we examined whether these signaling molecules trigger an intracellular Ca^{2+} response after integrin is engaged via sEV binding. Our results indicate that sEV-induced intracellular Ca^{2+} responses are markedly abrogated by inhibiting Src family kinase and PLCγ activity with PP2 and U73122, respectively, but not by their control analogs (Fig. 7e); therefore, sEV binding may activate Src family kinases and PLCγ to trigger the Ca^{2+} response.

Moreover, our findings were confirmed by single-molecule observation of PLCγ2, which showed that the number of PLCγ2 molecules recruited to the PM significantly increased immediately after sEV addition (within 1.5 min) and was reduced by treatment with PP2 but not with PP3 (Fig. 7f and g). Furthermore, the Ca^{2+} response was dramatically attenuated by an inhibitor of the IP_3 receptor (IP_3R) (Fig. 7e), demonstrating that the Ca^{2+} response occurs through IP_3R in the ER. In summary, these results suggest that PLCγ generates IP_3 from phosphatidylinositol bis(4,5)phosphate [$PI(4,5)P_2$] and that an increase in the cytosolic IP_3 concentration triggers the release of Ca^{2+} from the ER via IP_3Rs[43–45].

According to a previous report[46], the FAK autophosphorylation site Tyr-397 mediates binding with the C-terminal SH2 domain of PLCγ1. Building upon our aforementioned results, we hypothesized that Src-activated PLCγ molecules are recruited to FAK underneath sEVs bound to the PM. However, single molecules of FAK, PLCγ1, and PLCγ2 were not enriched in the PM underneath the sEVs (Fig. 7h), suggesting that the integrin and talin-1 clusters underneath the sEVs do not serve as platforms for FAK and PLCγ signaling. Conversely, single PLCγ2 molecules were frequently recruited to FAK clusters, as visualized by the PALM movie (Fig. 7i and j), suggesting that integrin adhesion signaling propagates from the sEV binding site to FAK clusters that are formed irrespective of sEV binding. Src family kinases might be involved in signal propagation; however, the detailed mechanisms underlying this process remain to be elucidated in future studies.

The sEV-induced Ca^{2+} response facilitates sEV uptake

Next, we examined the biological significance of the intracellular signals induced by sEV binding. Using the same experimental strategy in Fig. 3e, we found that sEV uptake into cells was considerably diminished after overexpression of the dominant negative mutant of talin-1, inhibition of PLCγ, Src family kinases, or IP_3R activity (Fig. 8a and b). Furthermore, the same treatment of the cells resulted in reduced uptake of dextran (Fig. 8c). These results explicitly showed that the uptake of sEVs and dextran is facilitated by the intracellular Ca^{2+} response induced by sEVs binding to the PM (Fig. 7). Although Fig. 3g and h explicitly shows that sEVs are internalized in a dynamin activity-dependent manner, Ca^{2+} does not directly regulate dynamin activity because dynamin does not contain a Ca^{2+}-binding site. Instead, a ubiquitously expressed Ca^{2+}-dependent phosphatase, calcineurin[47], is known to dephosphorylate dynamin, leading to enhanced GTPase activity of dynamin in a variety of cell types[48,49]. Thus, we used the calcineurin inhibitor FK506 to test whether calcineurin activates dynamin and facilitates the uptake of sEVs and dextran upon Ca^{2+} mobilization. Although sEV binding induced a normal Ca^{2+} response even after cells were treated with FK506 (Fig. 8d), the uptake of sEVs and dextran was largely reduced (Fig. 8b and c). These results equivocally show that the Ca^{2+} response induced by sEVs increases the activities of calcineurin and dynamin, facilitating sEV uptake.

Discussion

The mechanisms underlying the uptake of tumor-derived sEV by recipient cells have been poorly

elucidated[50]. To address this issue, we developed a cutting-edge super-resolution movie technique to visualize membrane invaginations in living cells with high spatial and temporal resolution and simultaneously performed single sEV particle imaging. In this study, first, we demonstrated the presence of distinct subtypes of tumor-derived sEVs (Fig. 1). Second, we discovered that all sEV subtypes derived from two distinct tumor cell types were internalized via phagocytosis, while some of sEV subtypes were also internalized via caveolae (Fig. 4 and 5). Intriguingly, sEVs, which were internalized via caveolae, exhibited smaller membrane defects than those of the other subtypes (Fig. 2) and induced raftophilic domains underneath them in the recipient cell PMs (Fig. 6). Third, surprisingly, we elucidated that paracrine sEV binding, rather than autocrine binding, triggered intracellular Ca^{2+} signaling (Fig. 7); this process was induced by adhesion signaling after integrin β1 and talin-1 clusters formed underneath the sEVs (Fig. 6 and 8e). The cluster formation induced the activation of Src family kinases and the recruitment of PLCγ2 to FAK clusters, which facilitated the digestion of $PI(4,5)P_2$ to produce IP_3 and led to Ca^{2+} mobilization through IP_3R in the ER (Fig. 7 and 8e). Increase of intracellular Ca^{2+} enhanced the dynamin activity through calcineurin, which facilitated the internalization of sEVs (Fig.3 and 8e). Only with our imaging technique, these stochastic molecular events were elucidated.

Several pathways for the internalization of sEVs, including clathrin-coated pits, caveolae, and phagocytosis, have been reported[51]. However, a consensus has not been reached regarding the predominant pathway involved, possibly due to difficulties in experimental methods[50]. For example, the bypass pathway can be overemphasized, as observed in knockout experiments in

which sEV uptake was enhanced in CAV1-KO cells[52]. A previous study by confocal microscopy reported that within minutes of addition, sEVs are internalized as single particles without accumulation from a specific site on the PM; however, the specific molecular mechanism involved has been unknown[53,54]. Therefore, it was necessary to directly observe and quantify sEV uptake by live recipient cells. Our state-of-the-art microscopic techniques with high temporal and spatial resolution enabled us to accurately determine the internalization pathway of distinct sEV subtypes in living recipient cells (Fig. 4 and 5) and unraveled the mechanism. Furthermore, although a recent review article proposed that sEV molecules may be redistributed to recycling endosomes in recipient cells[10], no direct evidence has been presented. Our results by 3D-dSTORM and single-particle imaging explicitly indicated that 20-40% of the internalized sEVs were transported into the recycling pathway (Fig. 5e and f), suggesting the following potential scenarios: either the internalized sEVs are re-secretion from the recipient cell surface or their membranes fuse, leading to the release of sEV cargos into the cytoplasm; in addition, membrane molecules, including integrins, are recycled on the recipient cell PMs (Fig. 8e).

Integrin cluster formation in the cell PM is known to trigger adhesion signaling that elicits intracellular calcium responses[36] and induces the recruitment of downstream molecules[34,55]. We observed the recruitment of PLCγ2 and the initiation of the Ca^{2+} response within 1-3 min after sEV addition, indicating that adhesion signaling is promptly initiated (Fig. 7). Notably, these prompt signaling events would lead to secondary signaling responses such as the release and functional expression of miRNAs and proteins following sEV uptake. To our

knowledge, the rapid and immediate signaling induced by sEVs, as observed in this study, has not been previously reported. For example, researchers have reported that tumor-derived sEVs containing PD-L1 interact with PD-1 expressed in T-cell PMs, resulting in the inhibition of T-cell activation[56,57]. However, cellular responses, such as the secretion of IL-2, were evaluated 24-48 h after sEVs were added. In addition, incubating WI-38 cells with 4175-LuT-derived sEVs increases the expression level of Src family kinases and their phosphorylation level in WI-38 cells[20]; however, these signals are not prompt because the expression level was examined in fixed cells 2 h after sEVs were added. Hence, this groundbreaking discovery explicitly demonstrates, for the first time, that the binding of tumor-derived sEVs promptly initiates intracellular signal transduction via adhesion molecules in the recipient cell PM. Furthermore, these signaling events were caused not only by tumor-derived sEVs but also by primary mesenchymal stem cell-derived sEVs (Fig. 7d), suggesting that signaling generally occurs immediately after sEVs bind to recipient cell PMs.

We discovered a novel mechanism by which paracrine sEV binding induces adhesion signals and facilitates their internalization (Fig. 8). This process involves the induction of intracellular Ca^{2+} mobilization by adhesion signaling, which enhances dynamin activity via calcineurin near the PM and promotes endocytosis[48,49] (Fig. 8e). Notably, fusion events between sEVs and recipient cell PMs were not observed, as shown in Fig. 3f. The internalization of sEVs by recipient cells is essential for incorporating bioactive components of sEVs into the cytosol and modifying the characteristics of recipient cells. Therefore, we successfully demonstrated the

physiological significance of sEV-induced signaling. However, the factors that cause the lack of intracellular signaling induced by autocrine sEV binding (Fig. 7d) remain unknown. As mentioned above, we found that integrin heterodimers in sEVs specifically bind to laminin on the recipient cell PM[27], and integrin heterodimer clusters likely occur on the cell PM and in sEVs across laminin (Fig. 6d). However, we observed that autocrine sEV binding does not induce intracellular signal transduction, suggesting that factors other than integrin heterodimers may be necessary for the initiation of intracellular signaling by sEVs. These factors should be elucidated in the future.

As mentioned, we elucidated the signaling pathway induced by paracrine sEV adhesion in detail. Interestingly, PLCγ2 molecules were recruited to FAK clusters, which differ from integrin and talin-1 clusters (Fig. 7i and j). FAK is known to be a scaffold protein that self-associates and interacts with cellular partners via its FERM domain[58]. These FAK clusters, also known as nascent adhesions, have recently been identified as synergistic liquid–liquid phase separated (LLPS) regions[59]. Therefore, PLCγ2 may function effectively in the PM by capitalizing on the LLPS structure (Fig. 8e). However, the mechanisms that underlie signal transduction from integrin and talin-1 clusters to FAK clusters have not been elucidated. Src family kinases act as downstream signaling molecules of integrin and talin-1, and Src activity is necessary for PLCγ2 recruitment[36]. Furthermore, previous studies have shown that the FAK cluster in B cells is also isolated from the BCR cluster, which serves as the signaling entry point, and that Src family kinases connect these signaling hubs[60]. Our results, combined with those of previous reports,

suggest that Src family kinases likely play pivotal roles in transmitting these signals. The specific underlying mechanisms should be elucidated in the future.

Thus, our study demonstrated that paracrine sEV binding induces adhesion signaling, which promptly triggers signal transduction at the recipient cell PM underneath sEVs. Increased intracellular Ca^{2+} facilitates the uptake of sEVs by recipient cells. These findings could lead to the use of a potential strategy to efficiently modify recipient cells by incorporating bioactive materials from sEVs. Moreover, this approach holds promise for future therapeutic applications.

References

1. Kalluri, R. & LeBleu, V. S. The biology, function, and biomedical applications of exosomes. *Science* 367, eaau6977 (2020).
2. Mathieu, M., Névo, N., Jouve, M., Valenzuela, J. I., Maurin, M., Verweij, F. J., Palmulli, R., Lankar, D., Dingli, F., Loew, D., Rubinstein, E., Boncompain, G., Perez, F. & Théry, C. Specificities of exosome versus small ectosome secretion revealed by live intracellular tracking of CD63 and CD9. *Nat. Commun.* 12, 4389 (2021).
3. Laulagnier, K., Javalet, C., Hemming, F. J., Chivet, M., Lachenal, G., Blot, B., Chatellard, C. & Sadoul, R. Amyloid precursor protein products concentrate in a subset of exosomes specifically endocytosed by neurons. *Cell. Mol. Life Sci.* 75, 757–773 (2018).
4. Mizenko, R. R., Brostoff, T., Rojalin, T., Koster, H. J., Swindell, H. S., Leiserowitz, G. S., Wang, A. & Carney, R. P. Tetraspanins are unevenly distributed across single extracellular vesicles and bias sensitivity to multiplexed cancer biomarkers. *J. Nanobiotechnology* 19, 1–17 (2021).
5. Van Niel, G., D'Angelo, G. & Raposo, G. Shedding light on the cell biology of extracellular vesicles. *Nat. Rev. Mol. Cell Biol.* 19, 213–228 (2018).
6. Han, C., Kang, H., Yi, J., Kang, M., Lee, H., Kwon, Y., Jung, J., Lee, J. & Park, J. Single-vesicle imaging and co-localization analysis for tetraspanin profiling of individual extracellular vesicles. *J. Extracell. Vesicles* 10, e12047 (2021).

7. Gonda, A., Kabagwira, J., Senthil, G. N. & Wall, N. R. Internalization of exosomes through receptor-mediated endocytosis. *Mol. Cancer Res.* 17, 337–347 (2019).

8. Möller, A. & Lobb, R. J. The evolving translational potential of small extracellular vesicles in cancer. *Nat. Rev. Cancer* 20, 697–709 (2020).

9. Marar, C., Starich, B. & Wirtz, D. Extracellular vesicles in immunomodulation and tumor progression. *Nat. Immunol.* 22, 560–570 (2021).

10. Gurung, S., Perocheau, D., Touramanidou, L. & Baruteau, J. The exosome journey: from biogenesis to uptake and intracellular signalling. *Cell Commun. Signal.* 19, 1–19 (2021).

11. Willms, E., Cabañas, C., Mäger, I., Wood, M. J. A. & Vader, P. Extracellular vesicle heterogeneity: subpopulations, isolation techniques, and diverse functions in cancer progression. *Front. Immunol.* 9, 738 (2018).

12. Kowal, J., Arras, G., Colombo, M., Jouve, M., Morath, J. P., Primdal-Bengtson, B., Dingli, F., Loew, D., Tkach, M. & Théry, C. Proteomic comparison defines novel markers to characterize heterogeneous populations of extracellular vesicle subtypes. *Proc. Natl. Acad. Sci. U. S. A.* 113, E968–E977 (2016).

13. Levet, F., Hosy, E., Kechkar, A., Butler, C., Beghin, A., Choquet, D. & Sibarita, J.-B. SR-Tesseler: a method to segment and quantify localization-based super-resolution microscopy data. *Nat. Methods* 12, 1065–1071 (2015).

14. Sato, Y., Kuwahara, K., Mogami, K., Takahashi, K. & Nishizawa, S. Amphipathic helical peptide-based fluorogenic probes for a marker-free analysis of exosomes based on

membrane-curvature sensing. *RSC Adv.* 10, 38323–38327 (2020).

15. Jensen, M. B., Bhatia, V. K., Jao, C. C., Rasmussen, J. E., Pedersen, S. L., Jensen, K. J., Langen, R. & Stamou, D. Membrane curvature sensing by amphipathic helices: a single liposome study using α-synuclein and annexin B12. *J. Biol. Chem.* 286, 42603–42614 (2011).

16. Kaiser, H.-J., Lingwood, D., Levental, I., Sampaio, J. L., Kalvodova, L., Rajendran, L. & Simons, K. Order of lipid phases in model and plasma membranes. *Proc. Natl. Acad. Sci. U. S. A.* 106, 16645–16650 (2009).

17. Tripathy, M., Thangamani, S. & Srivastava, A. Three-dimensional packing defects in lipid membrane as a function of membrane order. *J. Chem. Theory Comput.* 16, 7800–7816 (2020).

18. Schmid, S. L., McNiven, M. A. & Camilli, P. D. Dynamin and its partners: a progress report. *Curr. Opin. Cell Biol.* 10, 504–512 (1998).

19. Nanbo, A., Kawanishi, E., Yoshida, R. & Yoshiyama, H. Exosomes derived from Epstein-Barr virus-infected cells are internalized via caveola-dependent endocytosis and promote phenotypic modulation in target cells. *J. Virol.* 87, 10334–10347 (2013).

20. Hoshino, A., Costa-Silva, B., Shen, T. L., Rodrigues, G., Hashimoto, A., Tesic Mark, M., Molina, H., Kohsaka, S., Di Giannatale, A., Ceder, S., Singh, S., Williams, C., Soplop, N., Uryu, K., Pharmer, L., King, T., Bojmar, L., Davies, A. E., Ararso, Y., Zhang, T., Zhang, H., Hernandez, J., Weiss, J. M., Dumont-Cole, V. D., Kramer, K., Wexler, L. H.,

Narendran, A., Schwartz, G. K., Healey, J. H., Sandstrom, P., Labori, K. J., Kure, E. H., Grandgenett, P. M., Hollingsworth, M. A., de Sousa, M., Kaur, S., Jain, M., Mallya, K., Batra, S. K., Jarnagin, W. R., Brady, M. S., Fodstad, O., Muller, V., Pantel, K., Minn, A. J., Bissell, M. J., Garcia, B. A., Kang, Y., Rajasekhar, V. K., Ghajar, C. M., Matei, I., Peinado, H., Bromberg, J. & Lyden, D. Tumour exosome integrins determine organotropic metastasis. *Nature* 527, 329–335 (2015).

21. Kovtun, O., Dickson, V. K., Kelly, B. T., Owen, D. J. & Briggs, J. A. G. Architecture of the AP2/clathrin coat on the membranes of clathrin-coated vesicles. *Sci. Adv.* 6, 1–10 (2020).

22. Porta, J. C., Han, B., Gulsevin, A., Chung, J. M., Peskova, Y., Connolly, S., McHaourab, H. S., Meiler, J., Karakas, E., Kenworthy, A. K. & Ohi, M. D. Molecular architecture of the human caveolin-1 complex. *Sci. Adv.* 8, eabn7232 (2022).

23. Marion, S., Hoffmann, E., Holzer, D., Le Clainche, C., Martin, M., Sachse, M., Ganeva, I., Mangeat, P. & Griffiths, G. Ezrin promotes actin assembly at the phagosome membrane and regulates phago‐lysosomal fusion. *Traffic* 12, 421‐437 (2011).

24. Descloux, A., Grußmayer, K. S. & Radenovic, A. Parameter-free image resolution estimation based on decorrelation analysis. *Nat. Methods* 16, 918–924 (2019).

25. Nieves, D. J., Pike, J. A., Levet, F., Williamson, D. J., Baragilly, M., Oloketuyi, S., De Marco, A., Griffié, J., Sage, D., Cohen, E. A. K., Sibarita, J.-B., Heilemann, M. & Owen, D. M. A framework for evaluating the performance of SMLM cluster analysis algorithms.

Nat. Methods 20, 259–267 (2023).

26. Kemmoku, H., Takahashi, K., Mukai, K., Mori, T., Hirosawa, K. M., Kiku, F., Uchida, Y., Kuchitsu, Y., Nishioka, Y., Sawa, M., Kishimoto, T., Tanaka, K., Yokota, Y., Arai, H., Suzuki, K. G. N. & Taguchi, T. Single-molecule localization microscopy reveals STING clustering at the trans-Golgi network through palmitoylation-dependent accumulation of cholesterol. *Nat. Commun.* 15, 220 (2024).

27. Isogai, T., Hirosawa, K. M., Kanno, M., Yokota, Y. & Suzuki, K. G. N. Extracellular vesicles are bound to recipient cells predominantly by laminin-integrin association. *BioRxiv*, 1–23 (2024).

28. Strachan, L. R. & Condic, M. L. Cranial neural crest recycle surface integrins in a substratum-dependent manner to promote rapid motility. *J. Cell Biol.* 167, 545–554 (2004).

29. Parton, R. G. & Simons, K. The multiple faces of caveolae. *Nat. Rev. Mol. Cell Biol.* 8, 185–194 (2007).

30. Mayor, S., Rothberg, K. G. & Maxfield, F. R. Sequestration of GPI-anchored proteins in caveolae triggered by cross-linking. *Science* 264, 1948–1951 (1994).

31. Shi, F. & Sottile, J. Caveolin-1-dependent beta1 integrin endocytosis is a critical regulator of fibronectin turnover. *J. Cell Sci.* 121, 2360–2371 (2008).

32. Lu, F., Zhu, L., Bromberger, T., Yang, J., Yang, Q., Liu, J., Plow, E. F., Moser, M. & Qin, J. Mechanism of integrin activation by talin and its cooperation with kindlin. *Nat.*

Commun. 13, 2362 (2022).

33. Miranti, C. K. & Brugge, J. S. Sensing the environment: a historical perspective on integrin signal transduction. *Nat. Cell Biol.* 4, E83–E90 (2002).

34. Sawada, Y., Tamada, M., Dubin-Thaler, B. J., Cherniavskaya, O., Sakai, R., Tanaka, S. & Sheetz, M. P. Force sensing by mechanical extension of the Src family kinase substrate p130Cas. *Cell* 127, 1015–1026 (2006).

35. Bixby, J. L., Grunwald, G. B. & Bookman, R. J. Ca2+ influx and neurite growth in response to purified N-cadherin and laminin. *J. Cell Biol.* 127, 1461–1475 (1994).

36. Jones, N. P., Peak, J., Brader, S., Eccles, S. A. & Katan, M. PLCγ1 is essential for early events in integrin signalling required for cell motility. *J. Cell Sci.* 118, 2695–2706 (2005).

37. Johnsen, K. B., Gudbergsson, J. M., Andersen, T. L. & Simonsen, J. B. What is the blood concentration of extracellular vesicles? Implications for the use of extracellular vesicles as blood-borne biomarkers of cancer. *Biochim. Biophys. Acta* 1871, 109-116 (2019).

38. Jeppesen, D. K., Fenix, A. M., Franklin, J. L., Higginbotham, J. N., Zhang, Q., Zimmerman, L. J., Liebler, D. C., Ping, J., Liu, Q., Evans, R., Fissell, W. H., Patton, J. G., Rome, L. H., Burnette, D. T. & Coffey, R. J. Reassessment of exosome composition. *Cell* 177, 428–445.e18 (2019).

39. Joshi, B. S., De Beer, M. A., Giepmans, B. N. G. & Zuhorn, I. S. Endocytosis of extracellular vesicles and release of their cargo from endosomes. *ACS Nano* 14, 4444–4455 (2020).

40. Costa-Silva, B., Aiello, N. M., Ocean, A. J., Singh, S., Zhang, H., Thakur, B. K., Becker, A., Hoshino, A., Mark, M. T., Molina, H., Xiang, J., Zhang, T., Theilen, T. M., Garcia-Santos, G., Williams, C., Ararso, Y., Huang, Y., Rodrigues, G., Shen, T. L., Labori, K. J., Lothe, I. M., Kure, E. H., Hernandez, J., Doussot, A., Ebbesen, S. H., Grandgenett, P. M., Hollingsworth, M. A., Jain, M., Mallya, K., Batra, S. K., Jarnagin, W. R., Schwartz, R. E., Matei, I., Peinado, H., Stanger, B. Z., Bromberg, J. & Lyden, D. Pancreatic cancer exosomes initiate pre-metastatic niche formation in the liver. *Nat. Cell Biol.* 17, 816–826 (2015).

41. Sjaastad, M. D. & Nelson, W. J. Integrin‐mediated calcium signaling and regulation of cell adhesion by intracellular calcium. *BioEssays* 19, 47‐55 (1997).

42. Jakus, Z., Simon, E., Frommhold, D., Sperandio, M. & Mócsai, A. Critical role of phospholipase Cgamma2 in integrin and Fc receptor-mediated neutrophil functions and the effector phase of autoimmune arthritis. *J. Exp. Med.* 206, 577–593 (2009).

43. Maschek, B. J., Zhang, W., Rosoff, P. M. & Reiser, H. Modulation of the intracellular Ca2+ and inositol trisphosphate concentrations in murine T lymphocytes by the glycosylphosphatidylinositol-anchored protein sgp-60. *J. Immunol.* 150, 3198–3206 (1993).

44. Suzuki, K. G. N., Fujiwara, T. K., Edidin, M. & Kusumi, A. Dynamic recruitment of phospholipase C gamma at transiently immobilized GPI-anchored receptor clusters induces IP3-Ca2+ signaling: single-molecule tracking study 2. *J. Cell Biol.* 177, 731–742

(2007).

45. Suzuki, K. G. N., Fujiwara, T. K., Sanematsu, F., Iino, R., Edidin, M. & Kusumi, A. GPI-anchored receptor clusters transiently recruit Lyn and G alpha for temporary cluster immobilization and Lyn activation: single-molecule tracking study 1. *J. Cell Biol.* 177, 717–730 (2007).

46. Zhang, X., Chattopadhyay, A., Ji, Q. S., Owen, J. D., Ruest, P. J., Carpenter, G. & Hanks, S. K. Focal adhesion kinase promotes phospholipase C-gamma1 activity. *Proc. Natl. Acad. Sci. U. S. A.* 96, 9021–9026 (1999).

47. Rusnak, F. & Mertz, P. Calcineurin: form and function. *Physiol. Rev.* 80, 1483–1521 (2000).

48. Zhao, W.-D., Hamid, E., Shin, W., Wen, P. J., Krystofiak, E. S., Villarreal, S. A., Chiang, H.-C., Kachar, B. & Wu, L.-G. Hemi-fused structure mediates and controls fusion and fission in live cells. *Nature* 534, 548–552 (2016).

49. Davis, L. C., Morgan, A. J. & Galione, A. NAADP-regulated two-pore channels drive phagocytosis through endo-lysosomal Ca(2+) nanodomains, calcineurin and dynamin. *EMBO J.* 39, 1–23 (2020).

50. Mulcahy, L. A., Pink, R. C. & Carter, D. R. F. Routes and mechanisms of extracellular vesicle uptake. *J. Extracell. Vesicles* 3, 1–14 (2014).

51. Mathieu, M., Martin-Jaular, L., Lavieu, G. & Théry, C. Specificities of secretion and uptake of exosomes and other extracellular vesicles for cell-to-cell communication. *Nat.*

Cell Biol. 21, 9–17 (2019).

52. Svensson, K. J., Christianson, H. C., Wittrup, A., Bourseau-Guilmain, E., Lindqvist, E., Svensson, L. M., Mörgelin, M. & Belting, M. Exosome uptake depends on ERK1/2-heat shock protein 27 signaling and lipid Raft-mediated endocytosis negatively regulated by caveolin-1. *J. Biol. Chem.* 288, 17713–17724 (2013).

53. Heusermann, W., Hean, J., Trojer, D., Steib, E., Von Bueren, S., Graff-Meyer, A., Genoud, C., Martin, K., Pizzato, N., Voshol, J., Morrissey, D. V., Andaloussi, S. E. L., Wood, M. J. & Meisner-Kober, N. C. Exosomes surf on filopodia to enter cells at endocytic hot spots, traffic within endosomes, and are targeted to the ER. *J. Cell Biol.* 213, 173–184 (2016).

54. Tian, T., Zhu, Y. L., Hu, F. H., Wang, Y. Y., Huang, N. P. & Xiao, Z. D. Dynamics of exosome internalization and trafficking. *J. Cell. Physiol.* 228, 1487–1495 (2013).

55. Müller, P. M., Rademacher, J., Bagshaw, R. D., Wortmann, C., Barth, C., Van Unen, J., Alp, K. M., Giudice, G., Eccles, R. L., Heinrich, L. E., Pascual-Vargas, P., Sanchez-Castro, M., Brandenburg, L., Mbamalu, G., Tucholska, M., Spatt, L., Czajkowski, M. T., Welke, R.-W., Zhang, S., Nguyen, V., Rrustemi, T., Trnka, P., Freitag, K., Larsen, B., Popp, O., Mertins, P., Gingras, A.-C., Roth, F. P., Colwill, K., Bakal, C., Pertz, O., Pawson, T., Petsalaki, E. & Rocks, O. Systems analysis of RhoGEF and RhoGAP regulatory proteins reveals spatially organized RAC1 signalling from integrin adhesions. *Nat. Cell Biol.* 22, 498–511 (2020).

56. Chen, G., Huang, A. C., Zhang, W., Zhang, G., Wu, M., Xu, W., Yu, Z., Yang, J., Wang, B., Sun, H., Xia, H., Man, Q., Zhong, W., Antelo, L. F., Wu, B., Xiong, X., Liu, X., Guan, L., Li, T., Liu, S., Yang, R., Lu, Y., Dong, L., McGettigan, S., Somasundaram, R., Radhakrishnan, R., Mills, G., Lu, Y., Kim, J., Chen, Y. H., Dong, H., Zhao, Y., Karakousis, G. C., Mitchell, T. C., Schuchter, L. M., Herlyn, M., Wherry, E. J., Xu, X. & Guo, W. Exosomal PD-L1 contributes to immunosuppression and is associated with anti-PD-1 response. *Nature* 560, 382–386 (2018).

57. Poggio, M., Hu, T., Pai, C.-C., Chu, B., Belair, C. D., Chang, A., Montabana, E., Lang, U. E., Fu, Q., Fong, L. & Blelloch, R. Suppression of exosomal PD-L1 induces systemic anti-tumor immunity and memory. *Cell* 177, 414–427.e13 (2019).

58. Frame, M. C., Patel, H., Serrels, B., Lietha, D. & Eck, M. J. The FERM domain: organizing the structure and function of FAK. *Nat. Rev. Mol. Cell Biol.* 11, 802–814 (2010).

59. Case, L. B., De Pasquale, M., Henry, L. & Rosen, M. K. Synergistic phase separation of two pathways promotes integrin clustering and nascent adhesion formation. *eLife* 11, 1–36 (2022).

60. Shelby, S. A., Castello-Serrano, I., Wisser, K. C., Levental, I. & Veatch, S. L. Membrane phase separation drives responsive assembly of receptor signaling domains. *Nat. Chem. Biol.* 19, 750–758 (2023).

Figure legends

Figure 1

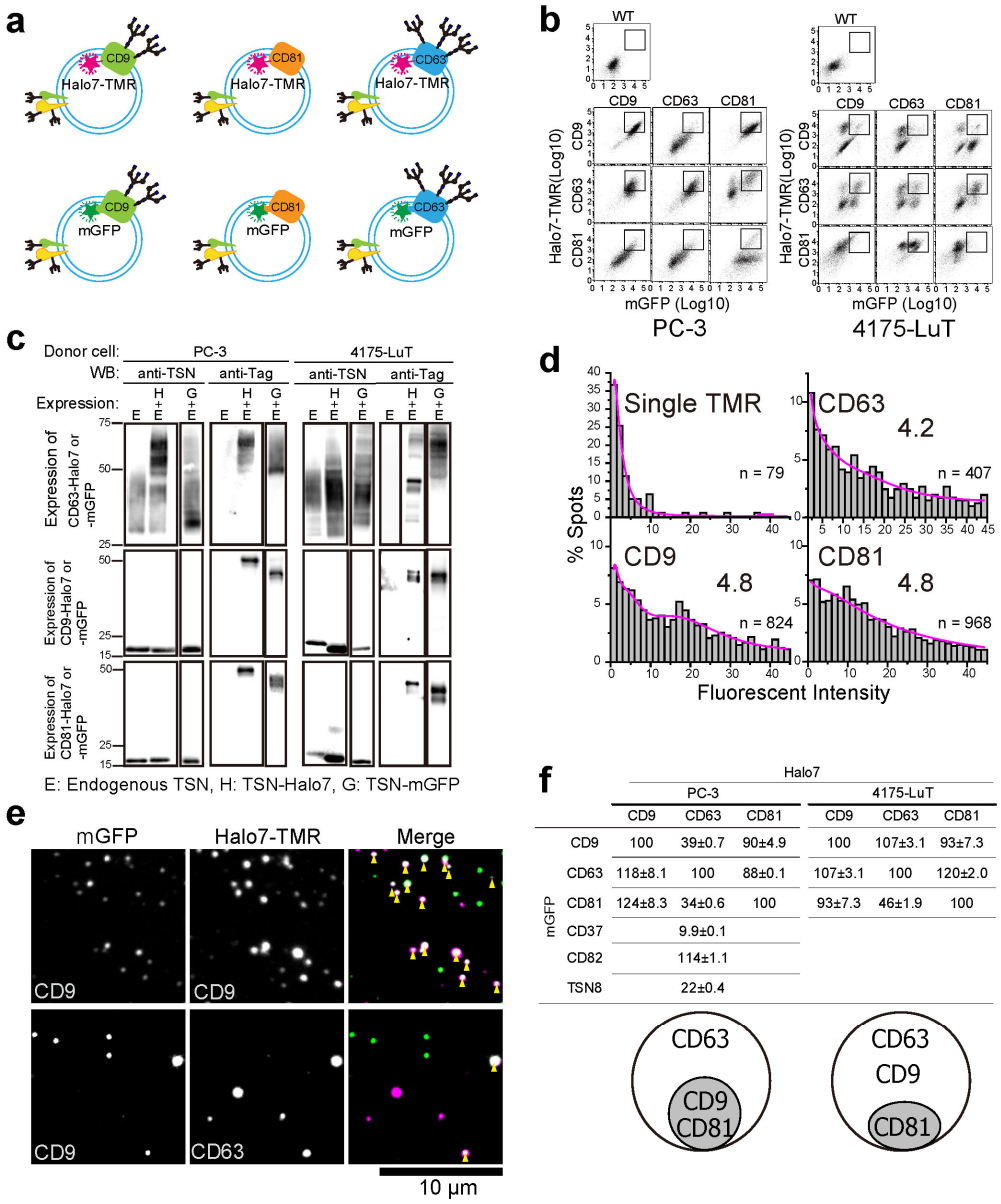

		Halo7					
		PC-3			4175-LuT		
		CD9	CD63	CD81	CD9	CD63	CD81
mGFP	CD9	100	39±0.7	90±4.9	100	107±3.1	93±7.3
	CD63	118±8.1	100	88±0.1	107±3.1	100	120±2.0
	CD81	124±8.3	34±0.6	100	93±7.3	46±1.9	100
	CD37		9.9±0.1				
	CD82		114±1.1				
	TSN8		22±0.4				

Fig. 1. Heterogenicity of sEVs. a, sEVs containing tetraspanin marker proteins. Three types of tetraspanins (CD9, CD63, and CD81) were fused with mGFP or Halo7-tag. b, Isolation of PC-3 or 4175-LuT cells expressing mGFP- and Halo7-labeled marker proteins using a cell sorter. Cells

within a rectangle on the plot were collected. c, Western blotting analysis of sEVs derived from PC-3 or 4175-LuT cells that express endogenous tetraspanin (TSN) and TSN-Halo7 or TSN-mGFP at the same density levels as those in the rectangle in b (the vertical axis for Halo7, the horizontal axis for mGFP). The cells were collected using a cell sorter. Western blotting was performed using antibodies against TSN, Halo7, or GFP. d, Distribution of the fluorescence intensities of tetraspanin-Halo7 labeled with TMR in individual sEV particles. The numbers in the graph indicate the average number of TMR molecules in one sEV particle. “n” indicates the number of examined sEV particles. e, Dual-color single-fluorescent particle images of sEVs on glass (green; mGFP, magenta; TMR). Double-stained sEV particles are indicated by yellow arrowheads. f, (top) Table summarizing the results obtained from the colocalization analysis of tetraspanins in sEVs. The numbers indicate the percentages of sEV particles with tetraspanins-Halo7-TMR (top row) containing tetraspanins-mGFP (left column). Calibrations of percentages were performed by observing the colocalization of the same tetraspanins stained with different dyes. (bottom) Venn diagram of the inclusion relationships of tetraspanins in sEVs.

Figure 2

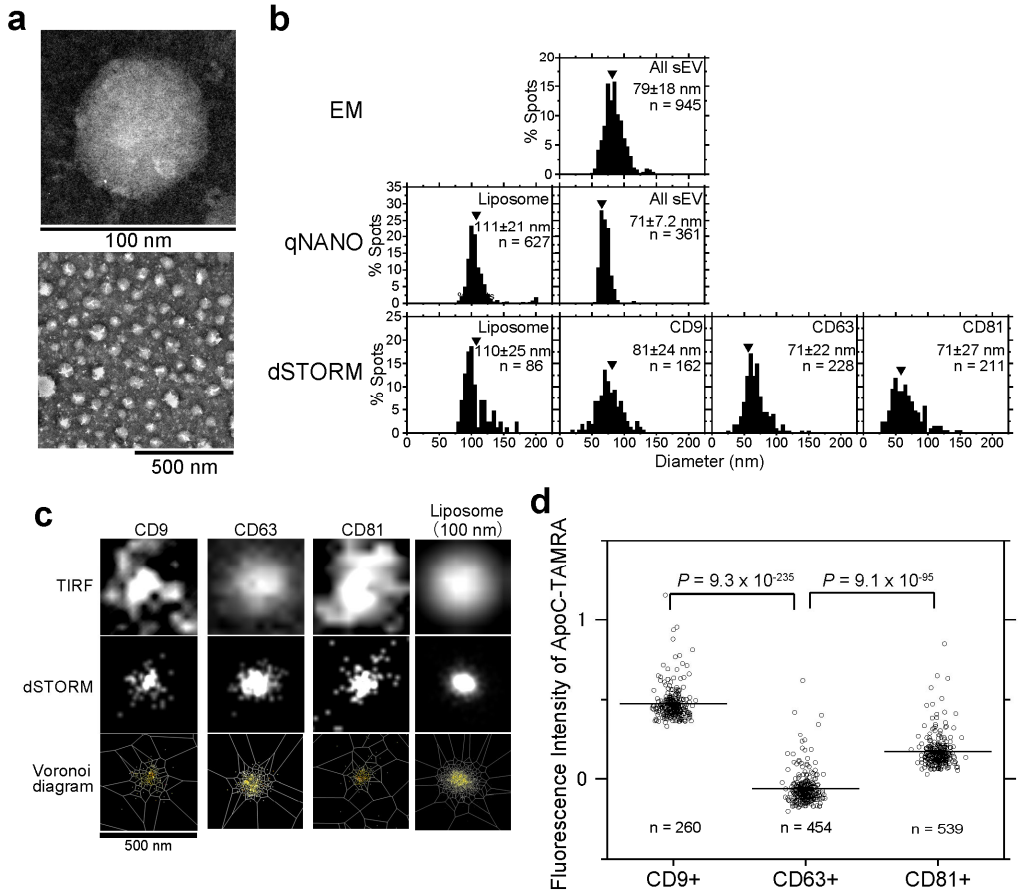

Fig. 2. sEV subtypes have similar diameters but different membrane defects. a, Magnified view (top) and wide-area view (bottom) of negatively stained TEM images of PC-3 cell-derived sEV particles. b, The diameters of sEVs determined by TEM (top), qNANO (middle), and dSTORM (bottom) methods. The numbers indicate the means ± SDs. "n" indicates the number of examined sEV particles derived from PC-3 cells. c, Size analysis using dSTORM. Typical images of an sEV containing CD9, CD63, and CD81 molecules stained with SF650B via Halo7 and a DMPC liposome containing GM3 conjugated with SF650B at the terminal sialic acid. dSTORM images

were determined using the Voronoi-based segmentation method (see Methods for details of the analysis). d, Distribution of the fluorescence intensities of ApoC-TAMRA on individual PC-3 cell-derived sEVs containing CD9, CD63, and CD81 labeled with SF650T via Halo7 isolated by ultracentrifugation. “n” indicates the number of examined sEV particles. The statistical test was performed by Welch’s t-test (two-sided).

Figure 3

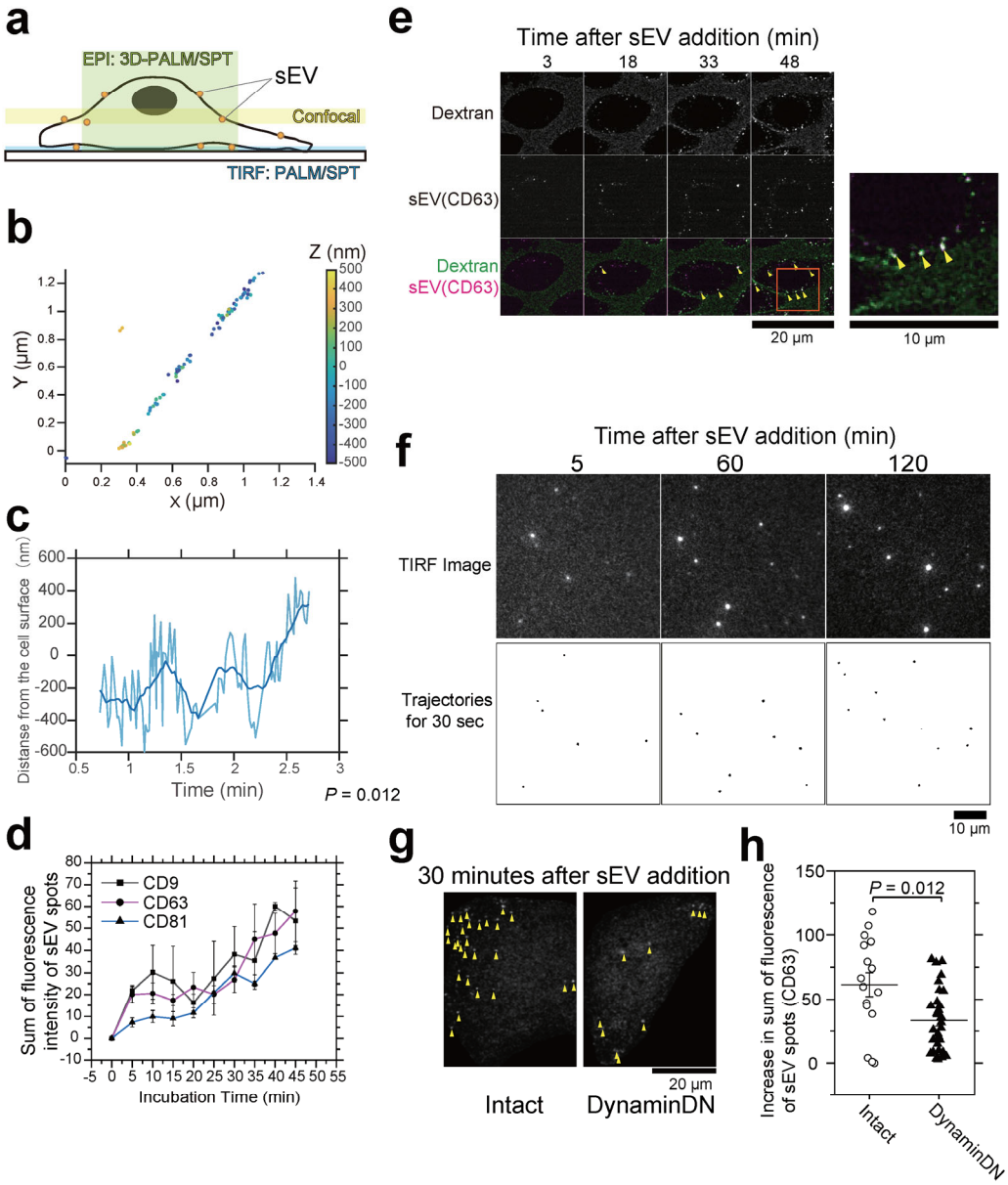

Fig. 3. Endocytosis of sEVs occurs via dynamin-regulated machinery. a, Intracellular regions observed by microscopy in this study. b, 3D trajectory of an sEV particle near the recipient cell PM. The coordinates in the z-direction are shown by color bar on the right. c, Time course of the

z-coordinate for the trajectory of an sEV particle shown in b. d, Time course for the sum of the fluorescence intensities of individual PC3 cell-derived sEV particles containing CD9-Halo7, CD63-Halo7, and CD81-Halo7 labeled with TMR in PZ-HPV-7 cells, which were measured by confocal microscopy. e, Confocal microscopy image sequences of pHrodo-Dextran and sEV-CD63Halo7-TMR at about 1.5 μm above the glass (left). After the internalization of pHrodo-Dextran, the fluorescence intensity of pHrodo is increased due to the decrease of pH in the surrounding environment, and fluorescent puncta appeared in cells with a dark background. Since pHrodo-Dextran was always present during the observation, pHrodo-Dextran emitted low-intensity fluorescence also outside of the cells. A magnified image of the orange rectangle in the merged image at 48 min after dextran/sEV was added (right). Colocalization between the puncta of pHrodo-Dextran and sEV-CD63Halo7-TMR is indicated by yellow arrowheads. f, Time series of single-molecule sensitivity TIRF images of sEVs containing mGFP-GPI attached to the recipient cell PM (upper) and trajectories of mGFP-GPI molecules for 30 sec (bottom). g, Representative single-particle image of sEV-CD63Halo7-TMR attached to an intact PZ-HPV-7 cell or a cell overexpressing a dynamin2 dominant negative mutant (DynaminDN). The sEV particles are indicated by yellow arrowheads. h, Increase in the sum of the fluorescence intensities of individual sEV-CD63Halo7-TMR particles in intact or DynaminDN-expressing PZ-HPV-7 cells 30 min after sEVs were added. The data are presented as the means ± SEs. The statistical analysis was performed by Welch's t-test (two-sided).

Figure 4

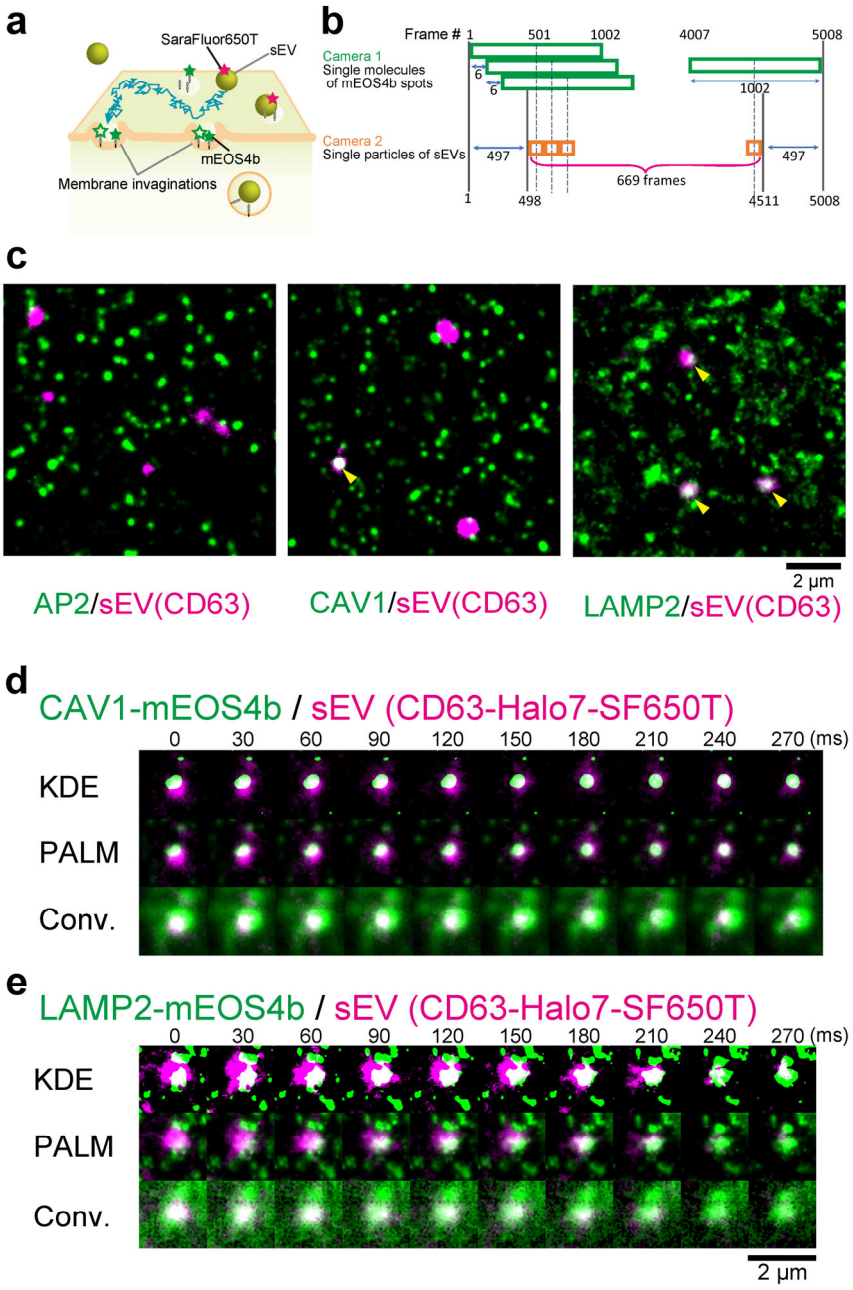

Fig. 4. Endocytosis of sEVs occurred on specific membrane invaginations. a, Schematic diagram showing the simultaneous real-time observation of single sEV particles and super-resolution microscopy images of membrane invaginations on living cell PMs. b, The method used to create

PALM movies of membrane invaginations superimposed with single-particle movies of sEVs. Data acquisition was performed by observing single-fluorescent molecules of mEOS4b at 200 frames/s (5,008 frames). The first PALM image was reconstructed using frames 1-1,002, which was then repeated by shifting the initial frames backward by 6 frames (30 ms), thus obtaining a total of 669 PALM images. These PALM still images were connected to form a “PALM movie”. The movies of single particles of sEVs were rolling-averaged for 6 frames and were synchronously merged with the PALM movie. c, Snapshots of PALM movies of membrane invaginations (green) merged with movies of single particles of sEVs (magenta). Colocalization events are indicated by yellow arrowheads. d, e, Image sequences of CAV1-mEOS4b/sEVs-CD63Halo7-SF650T (d) and LAMP2-mEOS4b/sEVs-CD63Halo7-SF650T (e). Single sEV particle images (magenta) merged with (top) binarized images of caveolae by the KDE method (green), (middle) PALM images, and (bottom) conventional fluorescence images.

Figure 5

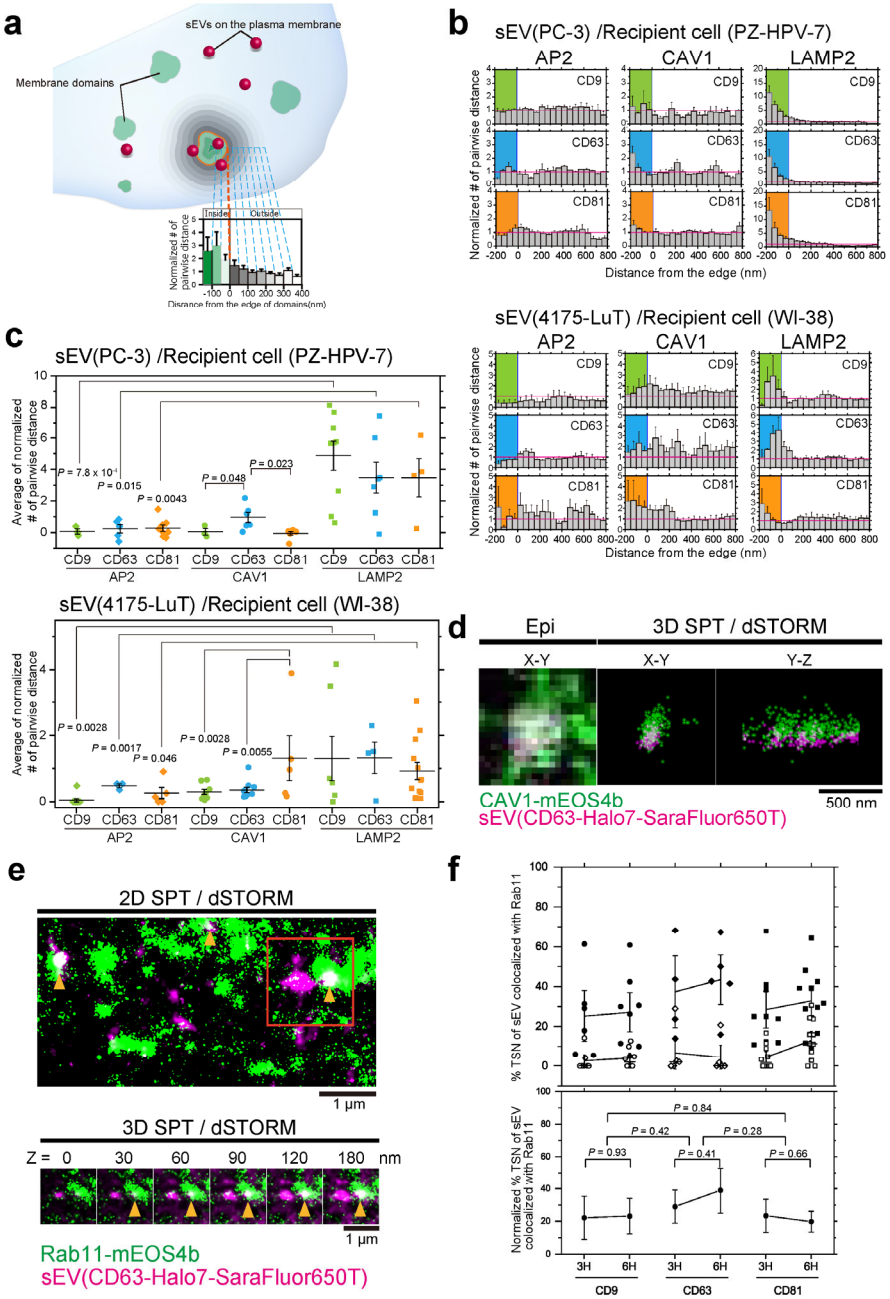

Fig. 5. Colocalization analysis of sEVs and membrane invaginations. a, Method used to analyze colocalization. The normalized relative frequency was defined as the ratio of the average value of the pair correlation function of actual images to that of randomly distributed spots generated by a

computer. Zero on the x-axis indicates the contour of the membrane area in the PALM images determined by the KDE method. When the sEVs are enriched in the membrane area, the normalized number of pairwise distances are greater than 1. b, Probability density analysis of sEVs and membrane invaginations. The colored areas indicate regions within the membrane invaginations. c, Enrichment of sEVs in membrane invaginations. The average value of the normalized number of pairwise distances from -200 to 0 nm in b was calculated for each cell and plotted in the graphs. The data are presented as the means ± SEs. d, 3D-dSTORM of CAV1-mEOS4b (green) and single-particle images of 4175-LuT cell-derived sEV-CD63Halo7-SF650T (magenta) in WI-38 cells. e, 2D/3D-dSTORM of Rab11-mEOS4b (green) and single-particle images of PC3 cell-derived sEVs-CD63Halo7-SF650T (magenta) in PZ-HPV-7 cells. Cropped z-section images (bottom) of the orange rectangle in the 2D projection image (top) are shown. The colocalization of sEV particles with Rab11-labeled recycling endosomes is indicated by yellow arrowheads. f, Degree by which sEV-tetraspanin (CD9, CD63, CD81)-Halo7-SF650T were colocalized with Rab11-mEOS4b, a recycling endosome marker. Closed and open symbols indicate the raw and randomized data, respectively (top). Net values were estimated by subtracting the randomized data from the raw data (bottom). The data are presented as the means ± SEs. The statistical test was performed by Welch's t-test (two-sided).

Figure 6

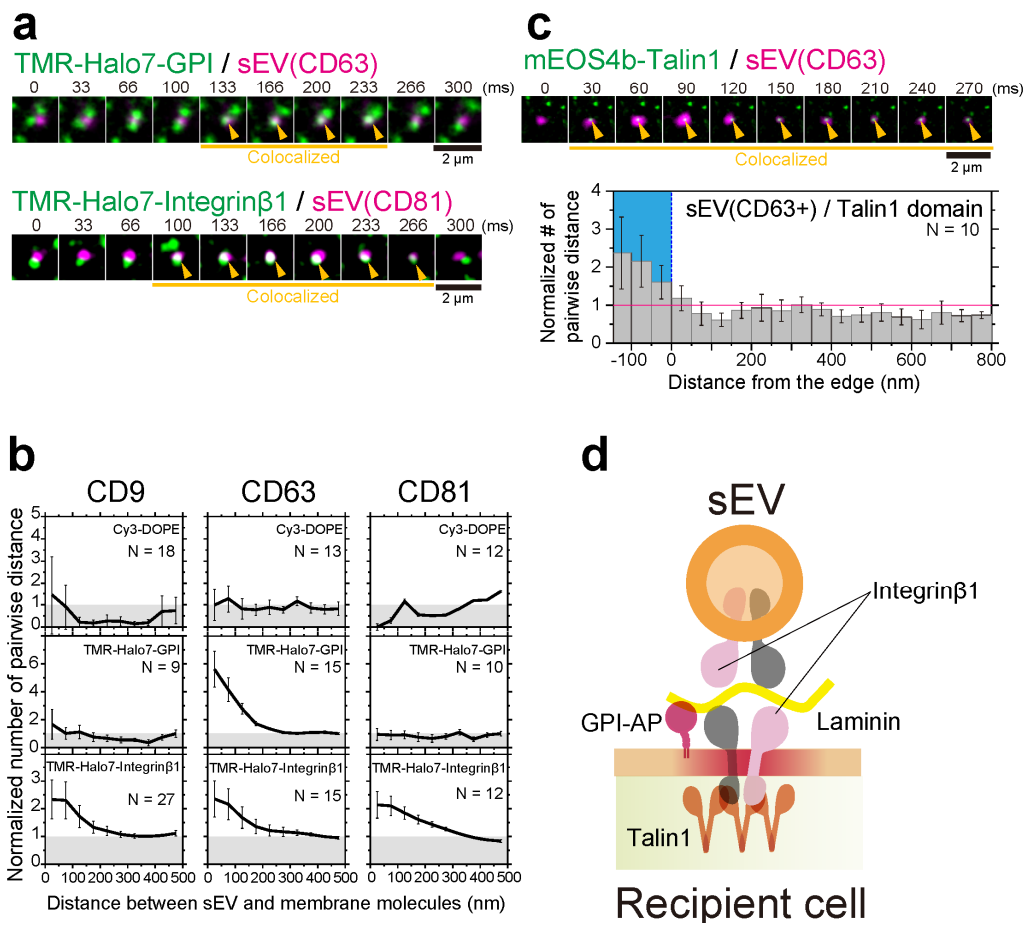

Fig. 6. Signaling platform induced by sEV binding to the PM of recipient cells. a, Image sequence (every 33 ms) of single molecules of TMR-Halo7-GPI (top) or TMR-Halo7-integrin β1 (bottom) and a single particle of sEV-CD63Halo7-SF650T on the living PZ-HPV-7 cell PM. Yellow arrowheads indicate colocalization events. b, Colocalization analysis of single sEV particles with single molecules of Cy3-DOPE, TMR-Halo7-GPI, or TMR-Halo7-integrin β1 in the cell PM. "N" indicates the number of examined cells. The data at each distance are presented as the means ± SEs. c, Talin1-enriched domains were induced underneath the sEVs. Image

sequence (every 30 ms) of the PALM image of mEOS4b-talin1 and a single sEV particle (top) and density analysis (bottom). “N” indicates the number of examined cells. The data at each distance are presented as the means ± SEs. d, Schematic diagram showing that integrin β1, talin-1, and GPI-anchored protein (GPI-AP) are enriched in the recipient cell PM underneath the sEV bound to laminin.

Figure 7

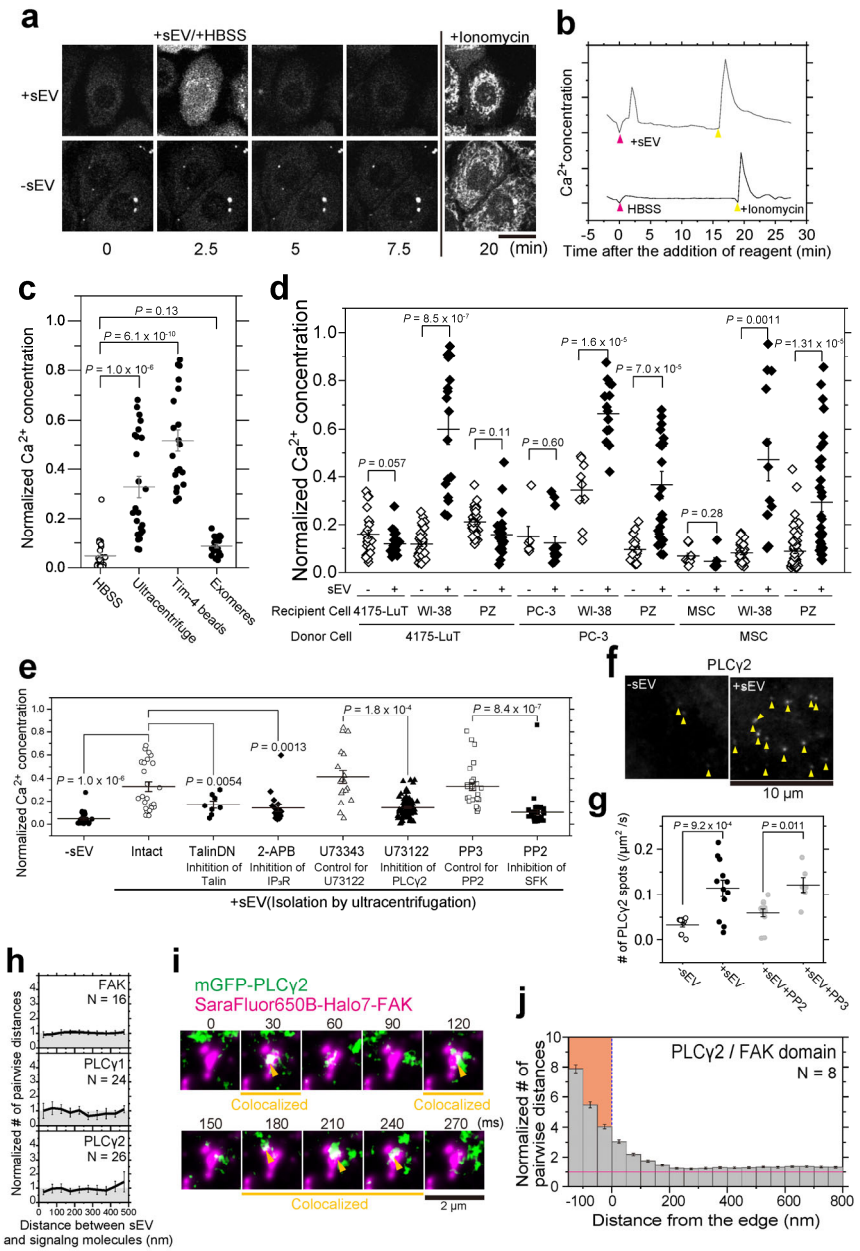

Fig. 7. sEV binding triggered intracellular Ca^{2+} signals. a, Confocal microscopy images of the Fluo-8H-loaded PZ-HPV-7 cells. sEVs (top) or HBSS (bottom) were added to the cells 2.5 min after the initial observation. Ionomycin was added to the cells 20 min after the initial observation. Scale bar: 20 μm. b, Time course of the fluorescence intensity of Fluo-8H in the

cells in a. c, Normalized Ca^{2+} concentration after the addition of HBSS, sEVs isolated by ultracentrifugation, those isolated by Tim-4 beads, and sEV-depleted culture medium (exomeres). d, Normalized Ca^{2+} concentration after the addition of sEVs (5.0×10^9 particles/ml at the final concentration) derived from 3 kinds of donor cells to 3 kinds of recipient cells (9 combinations). sEV(-) indicates the results obtained after exomeres were added. e, Normalized Ca^{2+} concentration of PZ-HPV-7 cells in which talin-1 activity was inhibited by expressing the dominant negative mutant (TalinDN) or the cells treated with an inhibitor of IP_3R (2-APB), PLC (U73122), SFK (PP2), a PLC control reagent (U73343) or SFK (PP3) after the addition of PC3 cell-derived sEVs. sEV(-) indicates the results obtained after exomeres were added. f, Single molecules of mGFP-PLCγ2 (indicated by yellow arrowheads) were frequently recruited to the PZ-HPV-7 cell PM within 90 sec after the addition of PC3 cell-derived sEV. g, Number of mGFP-PLCγ2 spots recruited to the PM before and after the sEVs were added in the absence/presence of PP2/PP3. h, Colocalization analysis of single sEV particles with single molecules of membrane-associated FAK, PLCγ1, and PLCγ2 in the cell PM. i, Image sequence (every 30 ms) of dSTORM images of SF650B-Halo7-FAK domains (magenta) and single molecules of mGFP-PLCγ2 (green). Yellow arrowheads indicate colocalization events. J, PLCγ2 molecules were frequently recruited to FAK-enriched domains. Density analysis of single molecules of mGFP-PLCγ2 on the SF650B-Halo7-FAK domains. Throughout Fig. 7, “N” indicates the number of examined cells, the data are presented as the means ± SEs, and the statistical tests were performed by Welch’s t-test (two-sided).

Figure 8

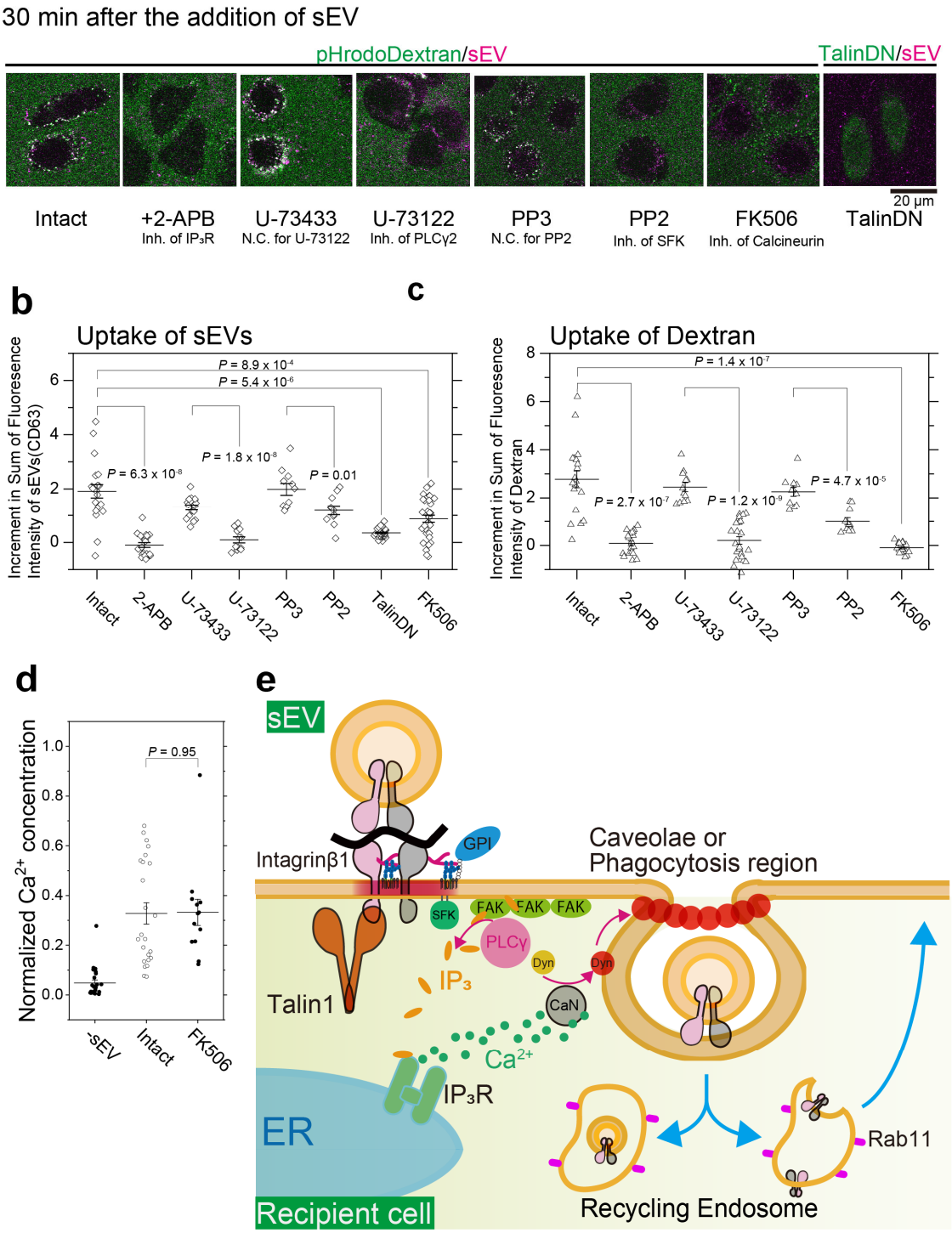

Fig. 8. sEVs induced intracellular signaling, which facilitated the endocytosis of sEVs. a, Typical

confocal microscopy images of the cells 30 min after the addition of pHrodo-Dextran (green) and sEV-CD63Halo7-TMR (magenta). Cells were treated with the following compounds or expressed a dominant negative mutant: an IP3R inhibitor (2-APB), a PLC control reagent (U73343), a PLC inhibitor (U73122), an SFK control reagent (PP3), an SFK inhibitor (PP2), a calcineurin inhibitor (FK506), or a dominant negative mutant of talin-1. As described in Fig. 3e legend, pHrodo-Dextran was present during the observation and emitted low-intensity fluorescence also outside of the cells, while after the internalization, the fluorescence intensity was increased due to the reduction of the pH and fluorescent puncta appeared in cells with a dark background. B, Increment in the sum of the fluorescence intensity of individual sEV-CD63Halo7-TMR particles in PZ-HPV-7 cells 30 min after sEVs were added. C, Increment in the sum of the fluorescence intensity of pHrodo-Dextran puncta in PZ-HPV-7 cells 30 min after sEVs were added. D, Normalized Ca^{2+} concentration in PZ-HPV-7 cells treated with or without 10 μM of the calcineurin inhibitor FK506 after the addition of HBSS (the same data as in Fig. 7d) or sEVs derived from PC-3 cells. e, Schematic diagram showing sEV endocytosis facilitated by intracellular signaling triggered by sEVs via integrin, talin-1, SFK, the FAK cluster, PLCγ, IP_3R, Ca^{2+}, calcineurin (CaN), and dynamin (Dyn).

Online methods

Cell culture

Human prostate cancer (PC-3; ATCC, CRL-1435) cells were cultured in HAM F12 medium (Sigma–Aldrich). MDA-MB-231 human breast cancer organotropic line 4175-LuT cells (kindly provided by Dr. Joan Massagué (Memorial Sloan Kettering Cancer Center (MSKCC), New York, NY, USA) were cultured in DMEM (Sigma–Aldrich). Human fibroblast (WI-38; ATCC, CCL-75) cells were cultured in MEM. The culture media for these 3 cell lines were supplemented with 10% FBS, 100 U/ml penicillin, and 100 μg/ml streptomycin (Gibco). Human prostate (PZ-HPV-7; ATCC, CRL-2221) cells were cultured in keratinocyte serum-free medium (Gibco) supplemented with 0.05 mg/ml bovine pituitary extract (Gibco) and 5 ng/ml human recombinant epidermal growth factor (Gibco). Human mesenchymal stem cells (MSCs; Lonza, PT-2501; Lot 23TL142784) were cultured in MSCGM (Lonza, PT-3238) supplemented with MSCGM single-quote supplements and growth factors (Lonza; PT-4105). Cells cultured for two to four passages were used for sEV collection or observation.

Preparation of cDNA plasmids, transfection, and incorporation of dyes

All plasmids used in this study were constructed with an NEBuilder HiFi DNA assembly system (New England Biolabs) and are listed in Supplementary Table 1. Wild-type PC-3 cells or 4175-LuT cells were transfected with cDNA encoding CD9, CD63, or CD81 tagged with mGFP or

Halo7 at the C-terminus (1000 ng cDNA) by using a 4D-nucleofector (LONZA) according to the following conditions. The transfection of PC-3 cells was performed using SF buffer, DS-150, and 4175-Lut cells using SE buffer, DS-130. Cells that stably expressed proteins tagged with Halo7 or mGFP were established by using G418 (0.2 mg/ml for PC-3 and 2 mg/ml for 4175-LuT) or blasticidin (2 mg/ml for PC-3 and 1 mg/ml for 4175-LuT), respectively. Cells that stably expressed appropriate amounts of the molecule of interest were selected using a flow cytometer (BD, FACSMelody). For observation of Cy3-DOPE on the PM, PZ-HPV-7 cells were incubated with 5 nM Cy3-DOPE in HBSS (200 μl) for 10 min at room temperature as reported previously[61].

Isolation of small extracellular vesicles from the cell culture supernatant

PC-3 cells, 4175-LuT cells, and MSCs were cultured in two 150-mm dishes and grown to approximately 100% confluence (1-2 × 10^7 cells), after which the cell culture medium was replaced with 30 ml of FBS-free medium (DMEM for MSCs). After 48 h of incubation, the cell culture supernatant was collected and subjected to centrifugation at 300×g for 10 min at 4 °C to remove cells. Next, to pellet debris and apoptotic bodies, the supernatant was centrifuged at 2,000×g and 4 °C for 10 min. Then, to pellet down large extracellular vesicles, the supernatant was centrifuged at 10,000×g and 4 °C for 30 min (himac CF16RN, T9A31 angle rotor, 50 ml Falcon tube). The supernatant was concentrated by ultrafiltration using a Centricon Plus 100K (Millipore). Subsequently, 800 μl of the collected small EVs (sEVs) were incubated with

HaloTag TMR ligand (Promega) (final concentration = 50 nM), HaloTag SF650T ligand (Goryo Chemical) (final concentration = 100 nM), or HaloTag SF650B ligand (final concentration = 100 nM) (Goryo Chemical) in PBS for 1 h at 37 °C. In the pellet-down method, sEVs were ultracentrifuged at 200,000×g and 4 °C for 4 h (with a himac CS100FNX, an S55A2 angle rotor, and S308892A microtubes for ultracentrifugation). The sEV pellets were resuspended in 200 µl of Hank's balanced salt solution (HBSS; Nissui) and observed through a microscope (1-5 × 10^9 particles/ml). For Western blotting, the pellet was resuspended in RIPA buffer containing Protease Inhibitor Cocktail Set III (Millipore). Alternatively, sEVs were also isolated from the cell culture supernatant using Tim4-affinity beads according to the manufacturer's protocol (Fujifilm-Wako Chemical Co.). Briefly, pretreatment before ultrafiltration was performed in the same manner as was performed with the ultracentrifugation method. Subsequently, Tim-4-bound magnetic beads were added to the supernatant, and the mixture was incubated for 1 h. The sEVs were washed, released by elution with chelating solution and diluted with PBS. To isolate exomeres, a small amount of sEVs remaining in the supernatant obtained by ultracentrifugation was removed by the Tim4-affinity method. All sEV samples were stored at 4 °C.

Transmission electron microscopy of sEVs after negative staining

The copper grid with the carbon-coated acetylcellulose film (EM Japan) was washed by a brief (~1 min) application of 10 µl of Milli-Q water, followed by blotting to remove excess liquid. The sEV sample (5 µl) was pipetted onto the grid and incubated for 1 min. Excess liquid was

removed by blotting. Five μl of 2% phosphotungstic acid (TAAB Laboratory and Microscopy) was briefly (~45 sec) placed on the grid, followed by blotting to remove excess liquid. The grid was dried in a desiccator containing silica gel desiccant at room temperature for 3 days and used for TEM observation. Images were acquired using a single TEM instrument (JEM-2100F, JEOL) at 200 kV. Images resulted from an average of 3-sec acquisitions on a side-mounted CCD camera (Gatan) and image solution software (Gatan Digital Micrograph).

Determination of the diameter of sEVs by qNano

The sEVs isolated as described above were dissolved in PBS. The diameter of the sEVs was measured by a tunable resistive pulse sensing instrument, qNano (Izon Science), according to the manufacturer's protocol. The data were analyzed by Izon Control Suite 3.3 (Izon Science). Measurements were performed with the following settings: an NP100 pore (particle detection range: 40-320 nm) with a stretch of 47 mm, a voltage of 1.2 V, and a pressure of 0.8 kPa. The samples were calibrated with 95 nm polystyrene calibration beads (Izon Science, CPC100).

Western blot analysis

The amounts of endogenous and tagged marker proteins (CD9, CD63, and CD81) in sEVs from PC-3 or 4175-LuT cells were determined by Western blotting. sEVs were suspended in RIPA buffer containing protease inhibitor cocktail set III (Millipore). The protein concentrations of the samples were determined by a BCA protein assay kit (Thermo Fisher Scientific) and adjusted to

1 mg/ml for SDS–PAGE. Then, 5x concentrated Laemmle's SDS sample buffer was added to the sample. After the mixture was incubated for 10 min at 70 °C in a block incubator, 20 µl of the mixture was loaded in the lanes of a precast 4-12% gradient polyacrylamide gel (Bolt Bis-Tris Plus Gels, Thermo Fisher Scientific). Molecular weights were determined using Precision Plus Protein Prestained Standards (Bio-Rad Laboratories). After electrophoresis, the proteins were transferred to a 0.45-µm polyvinylidene difluoride membrane (Millipore). The membranes were incubated in Blocking One solution (Nacalai Tesque) for 10 min at 4 °C and then incubated with antibodies against CD63 (1:1000; Cosmo Bio, SHI-EXO-M02), CD81 (1:1000; Santa Cruz, sc-166029), CD9 (1:1000; Abcam, ab263019), GFP (1:000; Sigma, SAB4301138), Halo (1:500; Promega, G9281) or β-actin (1:5000; Thermo Fisher Scientific, MA1-140) in Blocking One solution overnight. After washing with Tris-buffered saline (20 mM Tris and 150 mM NaCl, pH = 7.4) containing 0.1% Tween 20 (TBS-T), the membranes were incubated in Blocking One solution containing horseradish peroxidase (HRP)-conjugated goat anti-mouse IgG (1:5000, Millipore, 12-349), HRP-conjugated goat anti-rabbit IgG (1:10000, Sigma–Aldrich, A0545) or HRP-conjugated donkey anti-rabbit IgG (1:4000, Cytiva, NA934) for 1 h at room temperature. After washing with TBS-T, the membranes were treated with the ECL start reagent (GE Healthcare) or ECL select reagent (GE Healthcare) following the manufacturer's recommendations. The chemiluminescent images of the membranes were obtained by FUSION-SOLO.7S (Vilber-Loumat) and analyzed by ImageJ.

Cell treatments with various reagents

Src family kinase (SFK) activity was inhibited by treating the cells with 10 μM PP2 (Tokyo Kasei Kogyo:529573) for 10 min at 37 °C, and its analog, PP3 (Tokyo Kasei Kogyo:5334-30-5), was used as a control[62]. The IP_3R antagonist 2-APB (Wako, Japan)[63] was incubated at 10 μM for 10 min at 37 °C to inhibit store-operated release. PLCγ activity was inhibited by treatment with 6 μM U73122 (Cayman Chemical) for 15 min, and the analog U73343 (Cayman Chemical) was used as a control[64]. The GTPase activity of calcineurin was inhibited by treating the cells with 10 μM FK506 (Wako: 06306071)[49].

Determination of the number of sEVs bound to cell plasma membranes

PC-3 and 4175-LuT cell-derived sEVs containing CD63-Halo7 labeled with SF650T (sEV-CD63Halo7-SF650T) were incubated with PZ-HPV-7 and WI-38 cells cultured on a glass-based dish at 37 °C. The concentration of the fluorescently labeled sEVs was adjusted according to methods described in our recent report[27]. Briefly, glass windows of glass-based dishes were coated with 100 μl of 10 μg/ml anti-CD63 IgG antibody (8A12; Cosmo bio) in HBSS and then incubated for 2 h at 37 °C. Then, the antibody solution was removed, and the glass window was coated with 100 μl of 50 μg/ml casein (Sigma–Aldrich) in HBSS by incubation for 1 h at 37 °C to prevent nonspecific binding of the sEVs to the glass surface. One hundred μl of sEV-CD63Halo7-SF650T was placed in a glass window coated with an anti-CD63 IgG antibody and incubated for 1 h at 37 °C. After the solution was removed and washed twice with HBSS, the

single fluorescent particles of sEV-CD63Halo7-SF650T were observed with single-molecule detection sensitivity by TIRFM using a custom-built objective-lens-type microscope (based on an Olympus IX-83) equipped with a high-speed gated image intensifier (C9016-02MLG; Hamamatsu Photonics) coupled to an sCMOS camera (ORCA-Flash4.0 V2; Hamamatsu Photonics), and the number of sEVs on glass was measured. By observing the sEV particles at three different concentrations, we obtained a calibration curve, which enabled us to prepare identical concentrations of sEV solutions. The ExoSparkler Exosome Membrane Labeling Kit-Deep Red (Dojindo) was also used as a fluorescent probe for sEVs derived from PC-3 cells, 4175-LuT cells, and MSCs. sEVs were successfully labeled with Mem Dye-Deep Red following the Exosparkler Technical Manual. Subsequently, the fluorescently labeled sEVs were purified by the Tim-4 affinity method (Fujifilm Wako Chemical Co.).

Quantification of the number of fluorescent molecules in a single sEV

The mean (± SE) number of tetraspanins (CD9, CD63, and CD81) tagged with Halo7-TMR in single sEVs was determined from the distributions of signal intensities for individual fluorescent spots, which were observed by TIRFM using an in-house-built Olympus IX-83-based inverted microscope (100x 1.49 NA oil objective) equipped with two high-speed gated image intensifiers (C9016-02MLG; Hamamatsu Photonics) coupled to two sCMOS cameras (ORCA-Flash4.0 V2; Hamamatsu Photonics). The distributions of the fluorescence intensities of individual spots of TMR attached to the glass surface were fitted with a single log-normal function[61,65], representing

TMR monomers. The distributions of signal intensities of tetraspanins tagged with Halo7-TMR in individual sEV particles were subsequently fitted with the sum of the log-normal function for monomers, dimers, and greater oligomers, based on the monomer's log-normal function (10 mer was assumed to constitute the upper limit in this study)[66]. The percentages of each component were calculated and averaged. For the binding assay of TAMRA-conjugated amphipathic helix peptides (ApoC-TAMRA and α-synuclein(p2-23)-TAMRA), the fluorescence intensities of TAMRA on individual sEV particles containing CD9, CD63, and CD81-Halo7-SF650T were quantitatively analyzed via TIRFM using a Nikon Ti inverted microscope (100x 1.49 NA oil objective) equipped with two qCMOS cameras (ORCA Quest C15550-20UP; Hamamatsu Photonics).

Colocalization analysis of marker proteins in single sEVs

To examine whether tetraspanin marker proteins (CD9, CD63, and CD81) tagged with mGFP or Halo7-TMR are colocalized in the same sEV particle, we performed simultaneous dual-color observation of single sEV particles bound to the glass surface; these observations were performed by TIRFM with single-molecule detection sensitivity with a custom-built Olympus IX-83-based inverted microscope (100x 1.49 NA oil objective) equipped with two high-speed gated image intensifiers (C9016-02MLG; Hamamatsu Photonics) coupled to two sCMOS cameras (ORCA-Flash4.0 V2; Hamamatsu Photonics), as described previously[26,67]. The obtained sEV images were binarized by the "Li methods" function of ImageJ[68] for each channel, and the

number of sEV particles in the green channel (G) of mGFP, red channel (R) of Halo7-TMR, and merge of the two channels (M) (only colocalized spots exist in M) was counted by using the "Analyze Particles" function of ImageJ. The ratios of M to R (M/R) were quantitatively analyzed to eliminate effects caused by differences in the labeling efficiency of Halo7 with TMR.

Simultaneous dual-color observation of PALM movies of membrane invaginations and single-fluorescent particles of sEVs on living cell plasma membranes

PZ-HPV-7 or WI-38 cells expressing AP2α-mEOS4b, CAV1-mEOS4b, or LAMP2-mEOS4b were cultured on glass-based dishes for 2 days. After washing with HBSS 3 times, sEVs containing CD9, CD63, or CD81-Halo7-SF650T were incubated with the cells for 60 min at 37 °C. Single-fluorescent particles of the sEVs and single molecules of mEOS4b on the basal surface of the cells at 512 × 512 pixels (25.6 μm × 25.6 μm) were observed at 5 ms resolution (200 frames/s) for 5008 frames by TIRF illumination using a custom-built Olympus IX-83-based inverted microscope (100x 1.49 NA oil objective) equipped with two high-speed gated image intensifiers (C9016-02MLG; Hamamatsu Photonics) coupled to two sCMOS cameras (ORCA-Flash4.0 V2 Hamamatsu Photonics), as described previously[26,67]. Since the diameter of sEVs is approximately 70 nm, sEVs can enter the space between the basal membranes of cells and glass. The superimposition of images in different colors obtained by two separate cameras was performed as reported previously[45,67,69,70]. mEOS4b was activated and excited using a 405 nm laser (Excelsior-405C-50-CDRH, 50 mW, Spectra-Physics) and a 561 nm laser (Excelsior-561-

100-CDRW, 100 mW, Spectra-Physics) at 0.004 and 0.9 μW/μm^2, respectively, and SF650T was excited using a 647 nm laser (140 mW, Omicron Laserage Laserprodukte) at 3.2 μW/μm^2. Single-molecule tracking of mEOS4b and single-particle tracking of sEVs were performed by in-house computer software as previously reported[26,67,69,71–73]. The reconstructions of PALM images with a pixel size of 10 nm were performed using the ThunderSTORM plugin[74] for ImageJ installed in the Fiji package with "wavelet filtering" (B-spline order = 6 and B-spline scale = 6.0) and “least squares” (fitting radius = 3 pixels, initial sigma = 1.6 pixels). After spot detection, the postprocessing steps “Remove duplications” (distance threshold = uncertainty) and “Drift correction” (cross-correlation with 5 bins) were further performed. Subsequently, ThunderSTORM was used to output the frame, x and y coordinates of each spot as csv data, and these csv data were imported to a custom MATLAB program to create a super-resolution movie. In addition, we use the uncertainty, which represents the spatial precision of the spot. For each spot, a Gaussian distribution with the x and y coordinates as the center and a standard deviation (SD) equal to A (=6) times the uncertainty of the spot is generated as an existence probability distribution of the spot. The existence probability distribution for all structures at time t is obtained as a sum of all distributions for spots that appeared in [6t+1 6t+1002] frames. The PALM super-resolution movie data are generated by repeating this process for t=0, 1, 2, ⋯. To match the temporal resolution of a single-particle movie with that of a PALM movie and to preserve synchronicity, 6 consecutive frames in the single-particle movie were averaged, and the temporal resolution was converted to 33.3 frames/s. Subsequently, PALM images and 6-frame

averaged single-particle images were superimposed (Fig. 4b). Parameter-free image resolution estimation based on decorrelation analysis was performed using the Fiji plugin "Image Decorrelation Analysis"[24]. This software employs a Fourier-ring-correlation (FRC) method based on the calculation of the cutoff frequency of the correlation factor obtained for the original image and low-pass filtered images. This approach is used to estimate the resolution based on an individual image without further requirements or a priori knowledge[23].

Confocal microscopy

Confocal laser scanning fluorescence microscopy (CLSM) was performed at 37 °C with an FV1000-D microscope (Olympus IX81) equipped with an Ar laser (488 nm) and LED laser (559 nm). A 60× (numerical aperture (NA) = 1.46) oil objective was used to obtain images (typically, 1024 × 1024 pixels). The images were quantified and analyzed by the acquisition software FV10-ASW4.2 and ImageJ.

Intracellular Ca^{2+} imaging

Intracellular Ca^{2+} mobilization in living recipient cells was monitored by CLSM using Fluo8-H AM (AAT Bioquest) as a probe. The recipient cells in a glass-based dish were incubated with 5 μM Fluo-8H AM in HBSS (100 μl) in the dark for 30 min at 37 °C, after which the cells were washed three times with HBSS. Two hundred μl of sEV solution in HBSS was added to the cells. Images were acquired every 20 sec using CLSM, and observations were made for 10-20 cells in

each case. To measure the saturation level of the fluorescence signal intensity at high Ca^{2+} concentrations, 1 μM (final concentration) ionomycin (Fujifilm Wako Chemical Co.) was added (to increase the intracellular Ca^{2+} concentration to 1.3 mM of the extracellular Ca^{2+} concentration). The image sequences were analyzed using ImageJ software; time-dependent changes in the Fluo-8H signal intensity in the region of interest (ROI) (20-pixel diameter circle) were examined. Intracellular Ca^{2+} concentration induced by the addition of sEVs was normalized by that induced by 1 μM ionomycin (Fig. 7c-e and Fig. 8d).

Single-particle tracking and 3D super-resolution microscopy

To determine the 3D positions of sEVs containing tetraspanins labeled with SF650T via Halo7 and Cav1-mEOS4b or Rab11-mEOS4b in the cell PM or cytoplasm, single molecules/particles of these fluorescent probes in cells were observed by oblique-angle illumination (647 nm, 3.0 $\mu W/\mu m^2$ for observation at 33 ms/frame) using a Nikon Ti inverted microscope (100x 1.49 NA oil objective) equipped with two qCMOS cameras (ORCA Quest C15550-20UP; Hamamatsu Photonics). A cylindrical lens (MED54301, Nikon) was set in each imaging path to create astigmatism in two directions, allowing the x and y coordinates of the probe to be determined from the center of the image, as well as the z coordinate from the ellipticity[75]. To calibrate the Z position, we observed single particles of multicolor fluorescent beads (Tetrapeck Microspheres 100 nm in diameter; Thermo Fisher Scientific) fixed on a glass-based dish and continuously moved (1 nm/ms) using a Z-piezo stage (Nano Z100, Mad City Labs) at 5 ms/frame. The

obtained movies were analyzed by the “Cylindrical lens calibration” function of the ThunderSTORM plugin. The obtained xyz coordinates were plotted with MATLAB software. The typical localization precision values of the sEVs are shown in Extended Data Fig. 4. To quantitatively analyze the degree of colocalization between sEVs and Rab11, we first measured the center coordinates of the sEVs using the "Find Maxima" function of ImageJ. Next, we quantified the number density of Rab11-mEOS4b within a 100 nm radius around the center coordinates of the sEVs by ImageJ. To assess the degree of colocalization, we counted the number of sEVs that colocalized with Rab11-mEOS4b with a number density more than 2 times higher than the randomized background signal. The number of Rab11-mEOS4b molecules in a recycling endosome was 17.6±3.7 (mean ± SE), which was estimated by dividing the number of localizations of Rab11-mEOS4b in a recycling endosome for 5,002 frames by the number of localizations per mEOS4b molecule, as previously reported[26]. According to the Poisson distribution, all recycling endosomes contained more than one Rab11-mEOS4b molecule and were detectable by PALM.

Colocalization analysis between single molecules on the recipient cell PM and single sEV particles

To quantitatively analyze the colocalization of single molecules in the recipient PZ-HPV-7 cell PMs and single sEV particles, they were tracked with in-house computer software as previously reported[69,71]. The precision of the position determinations for single stationary fluorescent probes

in the observation at 5 ms/frame was estimated using the standard deviations obtained for the determined coordinates of the probes fixed on coverslips. For mGFP, TMR, and SF650T, the localization precisions of the single molecules were 26±1.0, 24±0.5, and 26±2.4 nm, respectively. We subsequently performed a pair cross-correlation analysis as follows. (1) An ROI was selected. (2) The distances between all pairs of green and red spots in the ROI in a video frame were measured, and this process was repeated for all the video frames in an image sequence (Extended Data Fig. 6a). (3) The number densities of pairwise distances R(r) were plotted against the distance (Extended Data Fig. 6b, top). (4) The cross-correlation function, C(r), was estimated by dividing R(r) by the number density of pairwise distances N(r) in the control image, which was obtained by superimposing the magenta image with the 180-degree rotated green image (Extended Data Fig. 6b, bottom).

Colocalization analysis between membrane invaginations in PALM movies and single sEV particles

The distances between the centroid of the sEVs and the contour of the membrane invaginations were quantified using single-particle tracking data of the sEVs and binarized images of the membrane invaginations in the PALM movies. To create binarized images of the membrane invaginations in the PALM movies, we used the kernel density estimation (KDE) method. KDE is a traditional image segmentation method that is used to rapidly determine the criterion for segmenting PALM images, as reported previously[26,76] and described below. Furthermore, a

recent study demonstrated that KDE is among the most appropriate methods for segmenting images of clearly outlined structures, such as protein clusters[25]. KDE provides a way to interpolate object boundaries without bias by randomly fluctuating activated boundary fluorophores.

ThunderSTORM datasets were imported into in-house KDE software (MATLAB) for image segmentation and colocalization analysis. We used localization coordinates as well as uncertainty, which reflects the spatial detection precision of the spots. Let x_i, y_i and $u_i, i = 1,2,\cdots,N$ be the horizontal and vertical localization coordinates and the uncertainty of spot i, respectively. N represents the total number of spots. Considering the uncertainty of the location measurement of spot i, the existence probability $p_i(x,y)$ of spot i spreads to the Gaussian distribution with the center coordinate x_i, y_i and the standard deviation (SD) that is proportional to the uncertainty u_i as follows:

$$p_i(x,y) = \frac{1}{2\pi(Au_i)^2} e^{-\frac{(x-x_i)^2+(y-y_i)^2}{2(Au_i)^2}}$$

in which A is the proportional coefficient of the SD to the uncertainty u_i; this coefficient was estimated as $A \approx 6$ in some preliminary experiments. The Gaussian distribution for constructing each existence probability $p_i(x,y)$ is called the Gaussian kernel. The existence probability distribution for all spots, i.e., the PALM image, is obtained by the average of the existence probability distribution $p_i(x,y)$ as follows:

$$p(x,y) = \alpha \frac{1}{N} \sum_{i=1}^{N} p_i(x,y) + (1-\alpha) p_{bg}(x,y)$$

excluding spots having extremely small or large uncertainties u_i because these spots are likely to be noise (e.g. electrical shot noise from camera). $p_{bg}(x, y)$ represents the background noise generated by the probability density distribution $f(v) = \frac{1}{2\pi\sigma_{bg}{}^2} e^{-\frac{(v-\mu_{bg})^2}{2\sigma_{bg}{}^2}}$, independent of x, y. α is a weight determined by the respective occurrence probabilities of the spots and background noise.

The structures can be considered to exist when the PALM image, which represents the probability of a structure existing, is above a certain threshold value θ because the spots appear uniformly inside the structures with a certain probability. The optimal threshold value θ must be determined for each obtained PALM image because the optimal value differs depending on the target molecule and the experimental environment. In general, the histogram of $p(x, y)$ values for all x, y forms a bimodal shape that contains larger values, which are created by dense spots in structures, and smaller values created by sporadic noise. Therefore, the threshold value θ should be determined to separate these two structures. Otsu's method is well known as a method for determining these threshold values[77]. Let S_{in} and S_{out} be sets of coordinates (x, y) where $p(x, y) \geq \theta$ and $p(x, y) < \theta$, respectively. The sets S_{in} and S_{out} indicate the inside and outside the clusters, respectively. The numbers of elements in sets S_{in} and S_{out} are represented by N_{in} and N_{out}, respectively. The intraclass variances of the sets S_{in} and S_{out} are calculated as follows:

$$\sigma^2[S_{in}] = \frac{1}{N_{in}} \sum_{(x,y)\in S_{in}} (p(x, y) - \mu[S_{in}])^2,$$

$$\sigma^2[S_{out}] = \frac{1}{N_{out}} \sum_{(x,y)\in S_{out}} (p(x,y) - \mu[S_{out}])^2.$$

In the above equations, $\mu[S_{in}]$ and $\mu[S_{out}]$ are the respective averages of the set S_{in} and S_{out} obtained by

$$\mu[S_{in}] = \frac{1}{N_{in}} \sum_{(x,y)\in S_{in}} p(x,y),$$

$$\mu[S_{out}] = \frac{1}{N_{in}} \sum_{(x,y)\in S_{out}} p(x,y).$$

The average of these intraclass variances is:

$$\sigma^2[S_{in}, S_{out}] = \frac{N_{in}\sigma^2[S_{in}] + N_{out}\sigma^2[S_{out}]}{N_{in} + N_{out}}.$$

Otsu's method determines the optimal threshold value $\hat{\theta}$ to minimize the average of the intraclass variances $\sigma^2[S_{in}, S_{out}]$ as follows:

$$\hat{\theta} = \arg\min_{\theta} \sigma^2[S_{in}, S_{out}].$$

In this study, the structures are determined using Otsu's method.

Thereafter, the distance from the contour of the determined structures to the center of the sEVs on the PM was measured, and the number densities of pairwise distances at a given distance were plotted. If an sEV is contained in a structure, the distance is displayed as a negative value. Furthermore, we also measured the distances between random coordinates and the contours of the structures in silico. The corresponding distributions of relative frequency were calculated using a bin width of 50 nm. For normalization, the relative frequency of sEVs within each bin was divided by the corresponding relative frequency of random spots. A ratio

exceeding 1 indicates a greater possibility of sEVs at the measured distance.

Estimation of sEV diameter by dSTORM

To estimate the sEV diameter, we acquired dSTORM images of sEVs that contained tetraspanins (CD9, CD63, and CD81) tagged with Halo7 SF650B attached to the glass. These images were attained by observing single molecules of SF650B for 10,000 frames by TIRF illumination (647 nm, 6.0 $\mu W/\mu m^2$ for observation at 4 ms/frame) using a Nikon Ti inverted microscope (100x 1.49 NA oil objective) equipped with a qCMOS camera (ORCA Quest C15550-20UP; Hamamatsu Photonics). dSTORM images with a pixel size of 10 nm were reconstructed using the ThunderSTORM plugin in ImageJ with "wavelet filtering" (B-spline order = 6 and B-spline scale = 6.0) and "least squares" (fitting radius = 3 pixels, initial sigma = 1.6 pixels). The obtained x and y coordinates for each spot in the csv data were subsequently imported into SR-Tesseler software[13] for cluster analysis based on Voronoi polygon density methods. To generate Voronoi polygons without correcting for blinking and multi-ON frame detection, the "Detection cleaner" function was used (within the entire ROI). The sEVs were identified using the "Objects" function with a Voronoi polygon density factor of 5. To ensure that the estimated sEV diameters were accurate, only sEVs with a minimum of 100 localizations were analyzed (Extended Data Fig. 2). Finally, the SR-Tesseler output data were plotted and subjected to statistical analysis using ORIGIN 2018b software.

Preparation of fluorescently labeled small unilamellar vesicles (SUVs)

As a size reference for sEVs, fluorescently labeled SUVs 100 nm in diameter were prepared according to the following protocol: 100 μl of 10 mM DMPC and 100 μl of 1 μM SF650B-GM3 were mixed in a chloroform solution in a brown vial and dried under nitrogen flow for 15 min, generating a thin lipid film on the bottom of the vial. The dried lipids were hydrated overnight in 1 ml of PBS (the final lipid concentration in the PBS suspension was 1 mM). The resulting multilamellar vesicles were freeze-thawed five times using liquid nitrogen and warm water at 45 °C. The vesicle suspension was extruded 10 times through a polycarbonate filter with 100 nm pores using a LiposoFast extruder (Avestin, Ottawa, Canada) immediately before use. The extruded vesicle suspension was diluted 100-fold with HBSS and attached nonspecifically to the glass surface.

Synthesis of ApoC-TAMRA and α-synuclein(p2-23)-TAMRA

Fmoc-protected amino acids were purchased from Watanabe Chemical Industries (Hiroshima, Japan) or FUJIFILM Wako Pure Chemical Co. (Tokyo, Japan). 5-TAMRA was purchased from Chemodex (Gallen, Switzerland). Probes were dissolved in DMSO to generate a 100 μM stock solution. The stock solution was stored in a freezer (−20°C) in the dark until further experiments. The final DMSO concentration in the ApoC-TAMRA-treated samples was less than 0.1% (v/v). ApoC-TAMRA (Supplementary Fig 1a-A) and α-synuclein(p2-23)-TAMRA (Supplementary Fig 1a-B) were synthesized using a Biotage Initiator and microwave peptide synthesizer (Biotage,

Uppsala, Sweden) based on Fmoc solid-phase peptide chemistry on Rink-Amide-ChemMatrix resin (Biotage). The 2-(6-chloro-1-H-benzotriazole-1-yl)-1,1,3,3-tetramethylaminium hexafluorophosphate (HCTU)/diisopropylethylamine (DIEA) system was employed for the coupling reaction. After all the amino acid residues were elongated, the AEEA spacer was introduced at the N-terminus, followed by coupling with TAMRA at the N-terminus. Deprotection and cleavage from the resin were conducted using trifluoroacetic acid/triisopropylsilane/water (95/2.5/2.5). The solution was dropped into cold diethyl ether to precipitate the crude peptide probe. The crude product was purified by a reverse-phase HPLC system (pump, PU-2086 Plus ×2; mixer, MX 2080-32; column oven, CO-1565; detector, UV-2070 plus and UV-1570 M (Japan Spectroscopic Co. Ltd., Tokyo, Japan)) equipped with a C18 column (Inertsil ODS3; GL Sciences Inc., Tokyo, Japan) using a gradient of water/acetonitrile containing 0.1% TFA (Supplementary Fig. 1b-A and b-B). The probe was verified by MALDI-TOF-MS (Bruker Daltonics Autoflex Speed-S1, Germany): MALDI-TOF-MS (ApoC-TAMRA) 3097.28 [calcd. for $(M+H)^+$: 3097.61], (p2-23-TAMRA): 2845.89 [calcd. for $(M+H)^+$: 2845.54] (Supplementary Table 2). The concentration of the probes was determined based on the molar absorption coefficient of TAMRA at 555 nm in DMSO ($\varepsilon = 90{,}000\ cm^{-1}M^{-1}$).

Synthesis of SaraFluor650B-GM3

Detailed information on the synthesis of SaraFluor650B-GM3 is provided in Supplementary Fig. 2. In brief, the prepared SaraFluor650B-linkerN_3 (S3) (Supplementary Fig. 2a) and BCN-GM3

(S5) products (Supplementary Fig. 2b) were dissolved in MeCN/H_2O (200 μl/100 μl) at room temperature. After the mixture was stirred for 19 h at room temperature, the reaction was monitored by TLC ($CHCl_3$/MeOH/5% $CaCl_2$ aq. = 5:3:0.2), and the reaction mixture was concentrated. The residue was purified by PTLC using $CHCl_3$/MeOH/H_2O (5:3:0.2) to generate SaraFluor650B-GM3 (S6).

Data availability

The datasets generated during and/or analyzed are available from the corresponding author upon reasonable request. Source data are provided in this paper.

Acknowledgements

We thank Dr. Tetsuya Hirata and Prof. Yasuhiko Kizuka (iGCORE, Gifu University) for supporting the cell sorter experiment. We also thank Yumi Matsuno for supporting the preparation of extracellular vesicles from donor cells; Shinobu Kawaguchi for constructing various cDNAs; Takahiro Fujiwara and Akihiro Kusumi for developing the analysis software for single-molecule imaging; Joan Massagué for providing 4175-LuT cells.

This work was supported in part by Japan Science and Technology Agency (JST) grants from the Core Research for Evolutional Science and Technology (CREST) program in the field of "Extracellular Fine Particles" to K.G.N.S., K.M.H., H.A. and Y.S. (JPMJCR18H2), the JST PRESTO program in the field of "Extracellular Fine Particles" to Y.S. (JPMJPR19H4), and Grants-in-Aid for Scientific Research from the Japan Society for the Promotion of Science (JSPS) (Kiban B to K.G.N.S. [21H02424, 18H02401]), a Grant-in-Aid for Challenging Research (Exploratory) from JSPS to K.G.N.S. (20K21387), a Grant for Core-to-Core program from JSPS to K.G.N.S. and H.A. (JPJSCCA202000007), a Grant-in-Aid for Innovative Areas from the Ministry of Education, Culture, Sports, Science and Technology of Japan (MEXT) to K.G.N.S. (18H04671), the National Cancer Center Research and Development Fund to K.G.N.S. (2023-A-03), the Takeda Science Foundation to K.G.N.S. and H.A., and the Uehara Memorial Foundation to K.G.N.S.

Author contributions

K.M.H. performed the single fluorescent-molecule tracking experiments and biochemical experiments. K.M.H., R.S.K., and K.G.N.S developed and constructed the single-molecule imaging station. Y.Y. and K.M.H. developed the analysis software. Y.S. synthesized the TAMRA-labeled AH peptide probes. E.Y., N.K., and H.A. synthesized the SaraFluor650T-labeled GM3 probes. A. H. provided the 4175-LuT cells. K.M.H., R.S.K., Y.S., A.H., and K.G.N.S. discussed the results and experimental plans extensively during the entire course of this research. K.M.H. and K.G.N.S. conceived and formulated the project and evaluated and discussed the data. K.M.H. and K.G.N.S. wrote the manuscript, and all authors participated in revising the manuscript.

Data and materials availability

All data are available in the main text or the supplementary materials. The computer programs and materials developed in house for use in this study are available upon request from the corresponding authors.

Competing interests statement

All the authors have no competing interests or conflicts of interest.

Extended data figure legends

Extended data Figure 1

a

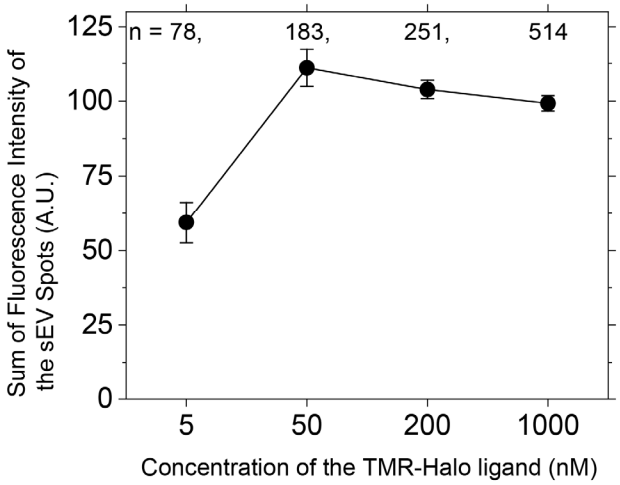

b

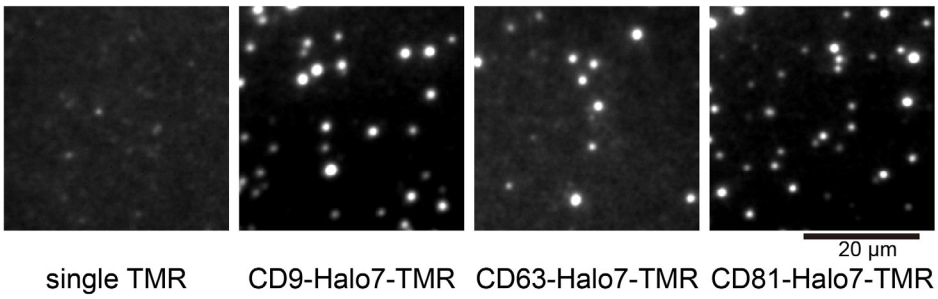

c

Number of Tetraspanin-Halo7-TMR (n)	Fraction of the sEVs (f)		
	CD9	CD63	CD81
1	0.040	0.055	0.040
2	0.095	0.120	0.096
3	0.152	0.176	0.153
4	0.182	0.192	0.183
5	0.175	0.168	0.175
6	0.139	0.123	0.139
7	0.095	0.077	0.095
8	0.057	0.042	0.057
9	0.030	0.020	0.030
10	0.015	0.009	0.014

Extended Data Fig. 1. Tetraspanin marker proteins in sEVs were labeled with TMR via Halo7 at high efficiency. a, Sum of the fluorescence intensities of the individual spots of sEVs containing CD63-Halo7 labeled with various concentrations of TMR Halo ligands after incubation for 1 h. The elevation of TMR-Halo ligand concentration above 50 nM did not increase the sum of the fluorescence intensities. As shown in the previous reports[61,67], these results indicate that the tetraspanin marker proteins were labeled with TMR via Halo7 at high efficiency. "n" indicates the number of examined particles. b, Typical images of single molecules of TMRs and individual PC-3 cell-derived sEV particles containing CD9-Halo7-TMR, CD63-Halo7-TMR, and CD81-Halo7-TMR. The expression levels of the tetraspanin-Halo7 proteins in sEVs derived from PC-3 cells are shown in Fig. 1c. c, Table shows the fractions (f) of sEVs containing the numbers (n) of tetraspanin-Halo7-TMR molecules indicated in the left column, which were estimated by fitting the histograms of fluorescence intensities of TMR in sEV particles with the lognormal function curves. The average numbers of tetraspanin-Halo7-TMR molecules per sEV particle were calculated by summing the values of $f \times n$.

Extended Data Figure 2

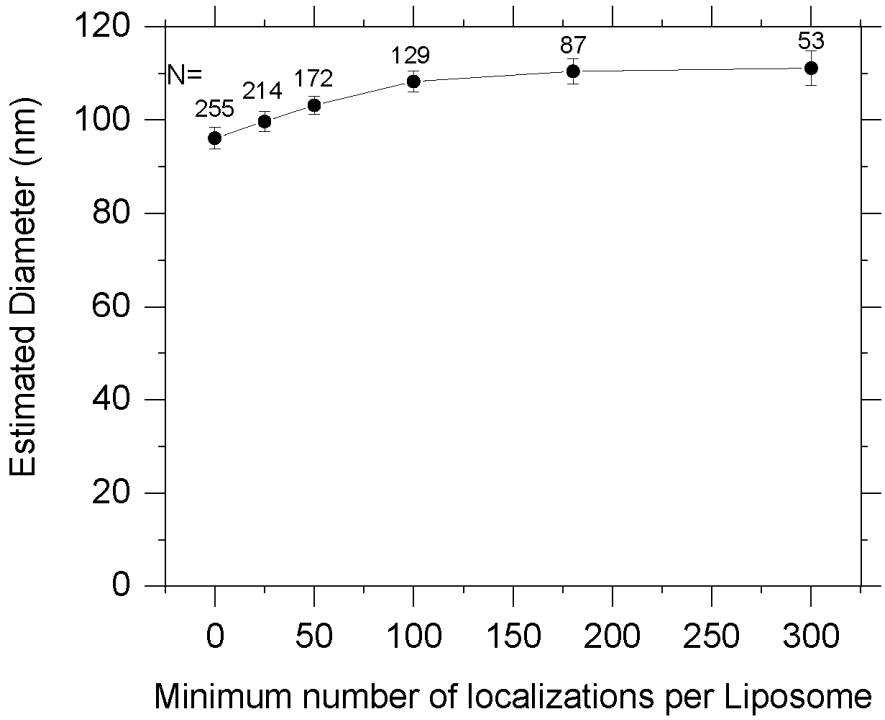

Extended Data Fig. 2. Estimation of the liposome diameter by dSTORM

The liposome diameter was estimated via the Voronoi method. Each number of localizations was obtained by dSTORM observation of SF650B-GM3 in liposomes. The x-axis indicates the minimum number of localizations used to estimate the diameter of each liposome. The estimated diameter was saturated above 100 localizations. “N” indicates the number of examined liposomes. The data are presented as the means ± SEs.

Extended Data Figure 3

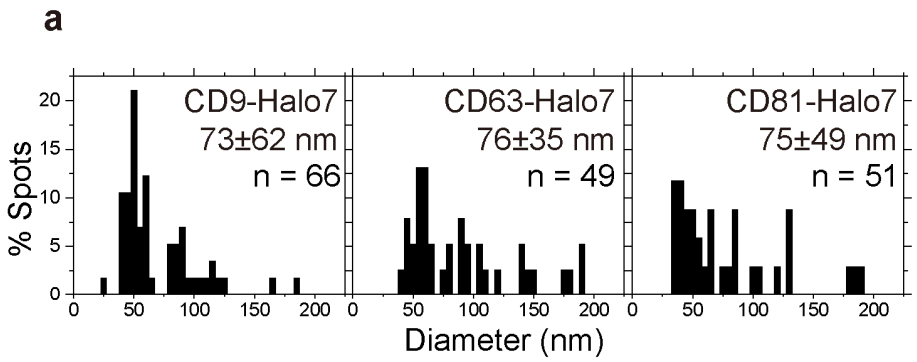

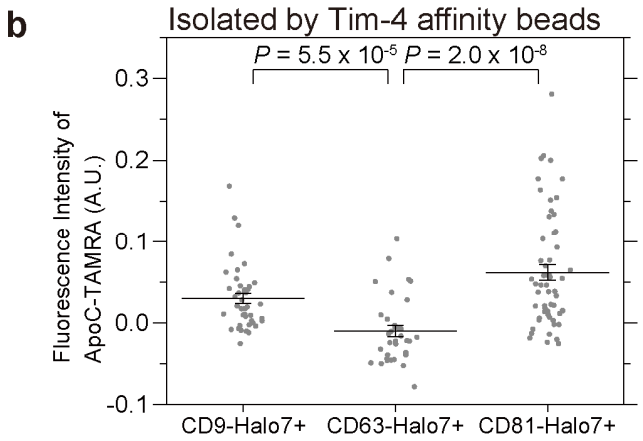

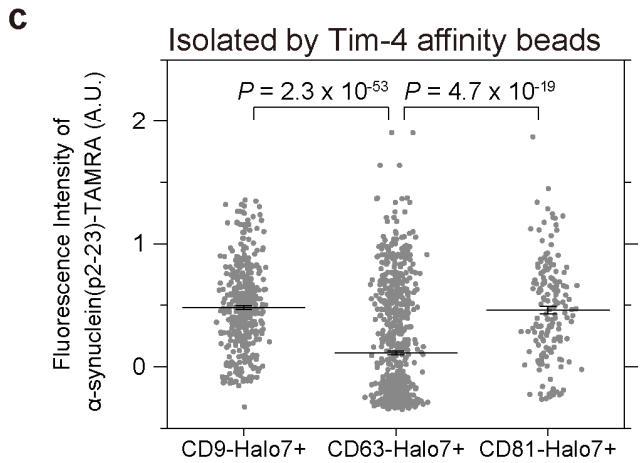

Extended Data Fig. 3. sEV subtypes isolated by the Tim-4 bead method exhibit different membrane defects. a, Diameter distributions of sEVs isolated by Tim-4 beads, which were determined by dSTORM methods. The data are presented as the means ± SDs. b, c, Distributions

of the fluorescence intensities of ApoC-TAMRA (b) and amphipathic helix peptide (p2-23) of α-synuclein (c) on the individual sEV particles that contained CD9, CD63, and CD81 labeled with SF650T via Halo7; these particles were isolated by the Tim-4 bead method. “n” indicates the number of examined particles. The data are presented as the means ± SEs, and the statistical tests were performed with Welch’s t-test (two-sided).

Extended Data Figure 4

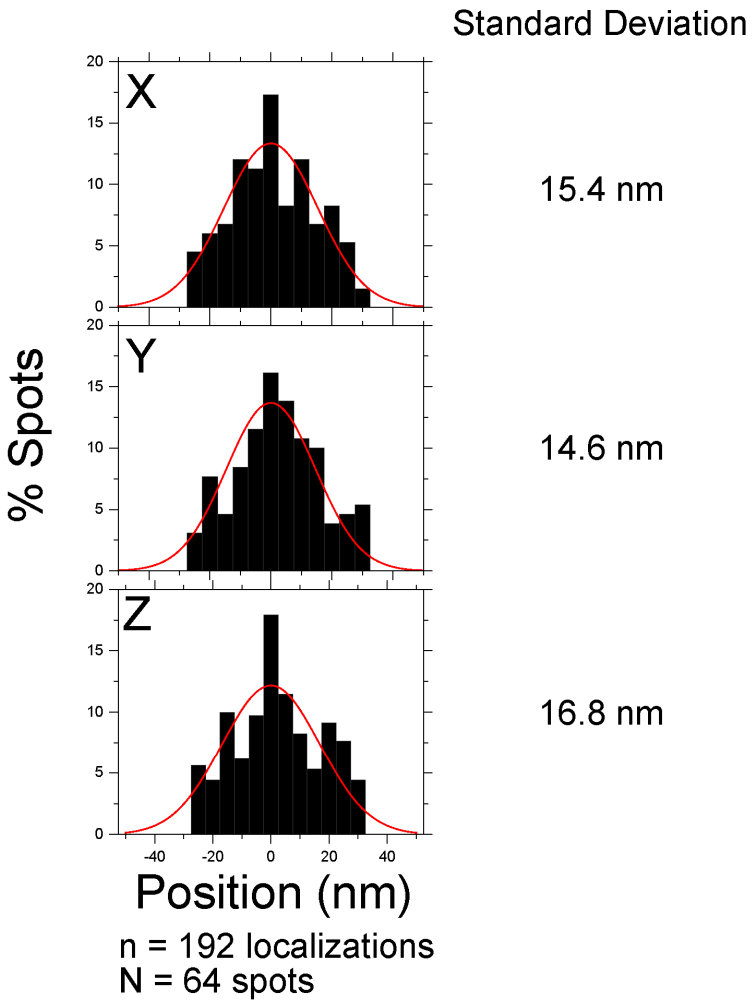

Extended Data Fig. 4. Accuracy of the position determined for single sEV particles sEV-CD63Halo7-SF650T particles were attached to coverslips and tracked in 3D. The center position and eccentricity were measured every 33 ms for 99 ms using ThunderSTORM software. Histograms of the displacements (n= 192 localizations) in the x-, y- and z-directions for all of the spots (N= 64) on the images were obtained. The histograms were fitted by Gaussian curves. The standard deviations in x-, y- and z-directions were 15.4, 14.6, and 16.8 nm, respectively.

Extended Data Figure 5

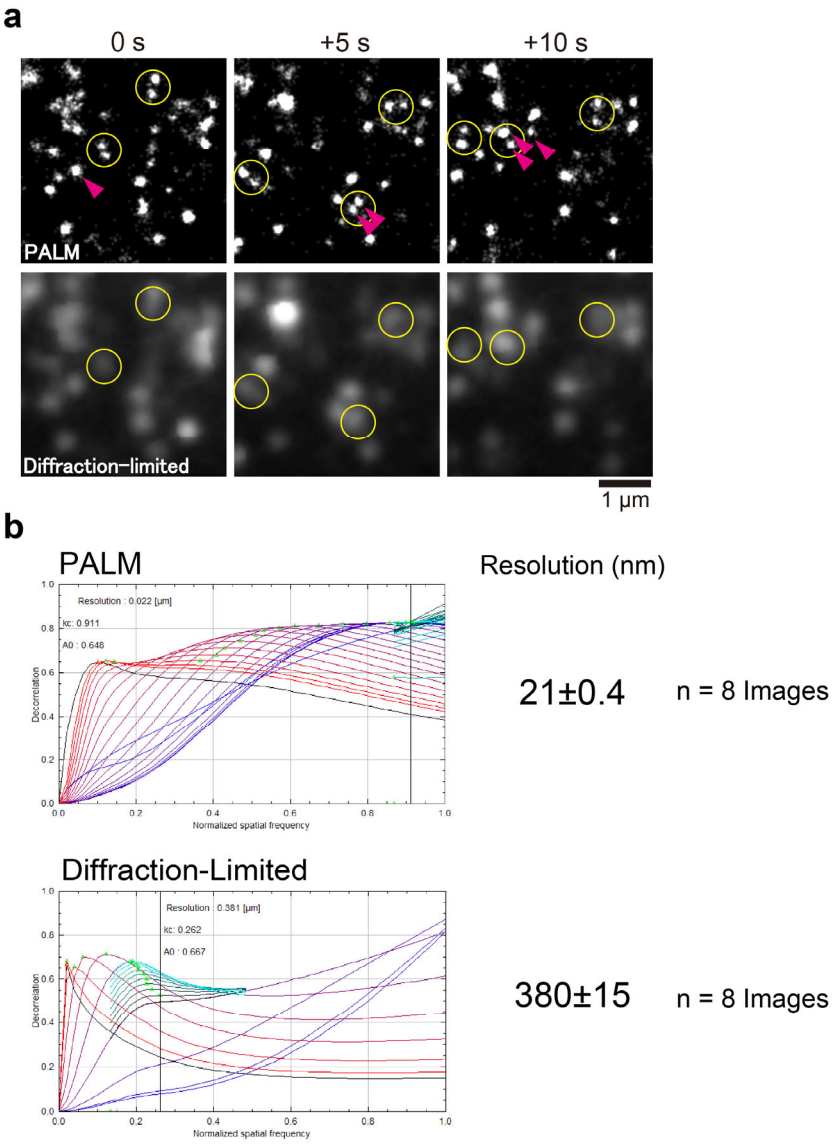

Extended Data Fig. 5. PALM image sequence obtained to track the dynamics of membrane structures. a, Typical PALM image sequence of caveolin-1 (Cav1)-mEOS4b in PZ-HPV-7 cells. Single molecules of Cav1-mEOS4b were observed at 5 ms/frame for 1002 frames (see Fig. 4b). The center coordinates of the spots were plotted to create a PALM image (top), and single fluorescent spots were superimposed (bottom). Caveolae in yellow circles can be resolved into

two in the PALM images but one in the diffraction-limited images. Caveolae marked by magenta arrowheads did not exist at the same position in the previous and/or next frame. b, Parameter-free image decorrelation analyses with Ng=50 and Nr=50.[24] Vertical gray lines: locations of kc, which is the cutoff frequency. Ng is the number of high-pass filters used to determine the resolution, and Nr is the number of points used to calculate the normalized frequency plots. The average spatial resolutions of 8 PALM images and 8 diffraction-limited images of caveolae were estimated to be 21 ± 0.4 nm and 380 ± 15 nm, respectively.

Extended Data Figure 6

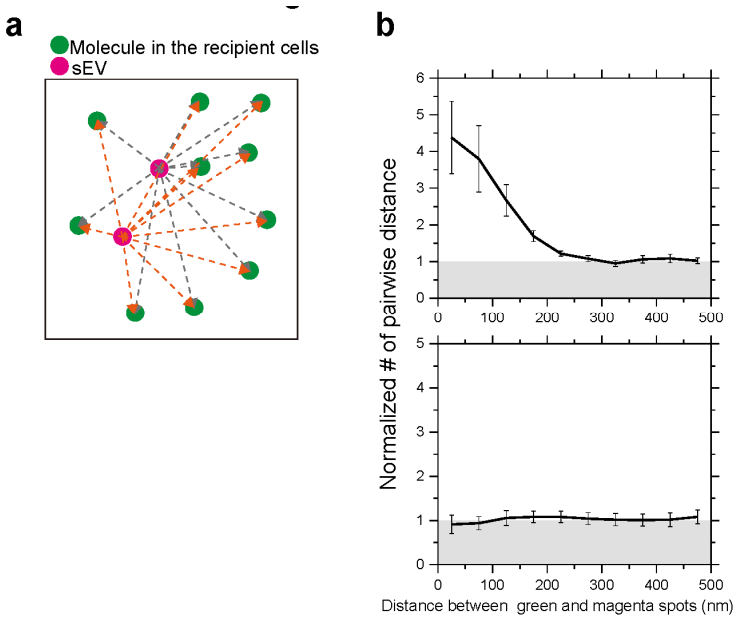

Extended Data Fig. 6. Correlation analysis of the fluorescent spots. a, In the movies showing simultaneous dual-color single-molecules, the spatial pair correlation function was determined and plotted in a histogram, showing the number densities of pairwise distances (the number of pairs normalized with the distance) at a given distance[78]. First, a region of interest (ROI) greater than 10 μm was selected, the distances between all the pairs of green and magenta spots in the ROI in a video frame were measured, and this process was repeated for all video frames in an image sequence. b, Distribution of the number of distances normalized for the unit area (i.e., the number density) for all the pairs was plotted against the distance. A bin size of 50 nm and an overall x-axis size of 500 nm were used throughout this study. This process was repeated for all sets of green and magenta videos, and the mean ± SE values were plotted (top). As a control, the magenta image was superimposed on the 180-degree rotated green image (bottom).

Extended Data Figure 7

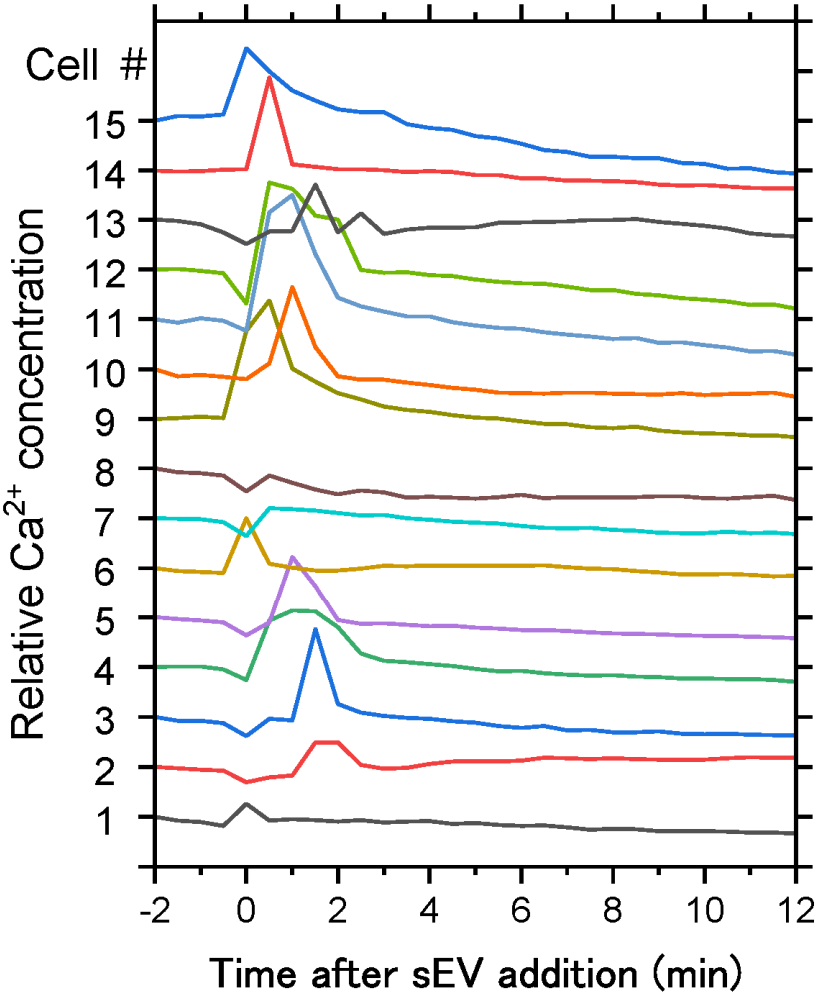

Extended Data Fig. 7. A transient increase in the intracellular Ca^{2+} concentration within a few minutes after PC3 cell-derived sEVs were added to PZ-HPV-7 cells.

Time course of the Fluo-8H fluorescence intensity in 15 representative cells.

Extended Data Figure 8

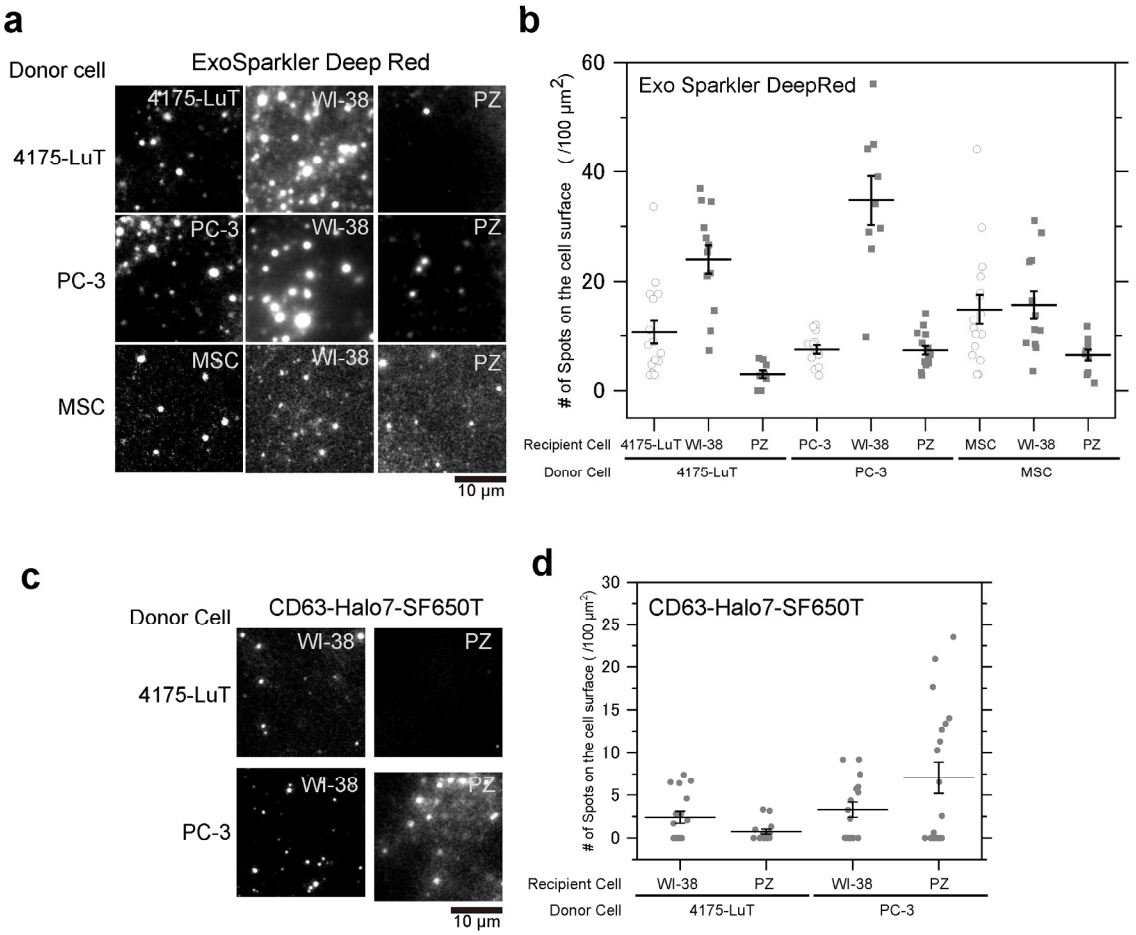

Extended Data Fig. 8. The binding affinity of sEVs to recipient cells was dependent on the cellular origin of the sEVs and the recipient cells. a, Typical TIRF images of sEVs labeled with ExoSparkler Deep Red bound to recipient cells 30 min after sEV addition. b, Number of sEV particles bound to the recipient cell PMs. Autocrine combinations of sEVs and recipient cells are shown as open circles. Paracrine combinations are shown in closed rectangles. c, Typical TIRF images of sEV-CD63Halo7-SF650T attached to recipient cells 30 min after its addition. d, Number of sEV particles on the cell surface for each combination of sEVs and recipient cells.

Online references

61. Suzuki, K. G. N., Kasai, R. S., Hirosawa, K. M., Nemoto, Y. L., Ishibashi, M., Miwa, Y., Fujiwara, T. K. & Kusumi, A. Transient GPI-anchored protein homodimers are units for raft organization and function. *Nat. Chem. Biol.* 8, 774–783 (2012).

62. Hanke, J. H., Gardner, J. P., Dow, R. L., Changelian, P. S., Brissette, W. H., Weringer, E. J., Pollok, B. A. & Connelly, P. A. Discovery of a novel, potent, and Src family-selective tyrosine kinase inhibitor. Study of Lck- and FynT-dependent T cell activation. *J. Biol. Chem.* 271, 695–701 (1996).

63. Maruyama, T., Kanaji, T., Nakade, S., Kanno, T. & Mikoshiba, K. 2APB, 2-aminoethoxydiphenyl borate, a membrane-penetrable modulator of Ins(1,4,5)P3-induced Ca^{2+} release. *J. Biochem.* 122, 498–505 (1997).

64. Macmillan, D. & McCarron, J. G. The phospholipase C inhibitor U-73122 inhibits Ca^{2+} release from the intracellular sarcoplasmic reticulum Ca^{2+} store by inhibiting Ca^{2+} pumps in smooth muscle. *Reassess. Exosome Compos.* 160, 1295–1301 (2010).

65. Meckel, T., Semrau, S., Schaaf, M. J. M. & Schmidt, T. Robust assessment of protein complex formation in vivo via single-molecule intensity distributions of autofluorescent proteins. *J. Biomed. Opt.* 16, 076016 (2011).

66. Tsunoyama, T. A., Watanabe, Y., Goto, J., Naito, K., Kasai, R. S., Suzuki, K. G. N., Fujiwara, T. K. & Kusumi, A. Super-long single-molecule tracking reveals dynamic-

anchorage-induced integrin function. *Nat. Chem. Biol.* 14, 497–506 (2018).

67. Morise, J., Suzuki, K. G. N., Kitagawa, A., Wakazono, Y., Takamiya, K., Tsunoyama, T. A., Nemoto, Y. L., Takematsu, H., Kusumi, A. & Oka, S. AMPA receptors in the synapse turnover by monomer diffusion. *Nat. Commun.* 10, 5245 (2019).

68. Li, C. H. & Tam, P. K. S. An iterative algorithm for minimum cross entropy thresholding. *Pattern Recognit. Lett.* 19, 771–776 (1998).

69. Komura, N., Suzuki, K. G. N., Ando, H., Konishi, M., Koikeda, M., Imamura, A., Chadda, R., Fujiwara, T. K., Tsuboi, H., Sheng, R., Cho, W., Furukawa, K., Furukawa, K., Yamauchi, Y., Ishida, H., Kusumi, A. & Kiso, M. Raft-based interactions of gangliosides with a GPI-anchored receptor. *Nat. Chem. Biol.* 12, 402–410 (2016).

70. Fujiwara, T. K., Takeuchi, S., Kalay, Z., Nagai, Y., Tsunoyama, T. A., Kalkbrenner, T., Iwasawa, K., Ritchie, K. P., Suzuki, K. G. N. & Kusumi, A. Development of ultrafast camera-based single fluorescent-molecule imaging for cell biology. *J. Cell Biol.* 222, e202110160 (2023).

71. Kinoshita, M., Suzuki, K. G. N., Matsumori, N., Takada, M., Ano, H., Morigaki, K., Abe, M., Makino, A., Kobayashi, T., Hirosawa, K. M., Fujiwara, T. K., Kusumi, A. & Murata, M. Raft-based sphingomyelin interactions revealed by new fluorescent sphingomyelin analogs. *J. Cell Biol.* 216, 1183–1204 (2017).

72. Suzuki, K. G. N., Kasai, R. S., Fujiwara, T. K. & Kusumi, A. Single-molecule imaging of receptor–receptor interactions. *Methods Cell Biol.* 117, 373–390 (2013).

73. Fujiwara, T. K., Tsunoyama, T. A., Takeuchi, S., Kalay, Z., Nagai, Y., Kalkbrenner, T., Nemoto, Y. L., Chen, L. H., Shibata, A. C. E., Iwasawa, K., Ritchie, K. P., Suzuki, K. G. N. & Kusumi, A. Ultrafast single-molecule imaging reveals focal adhesion nano-architecture and molecular dynamics. *J. Cell Biol.* 222, e202110162 (2023).

74. Ovesný, M., Křížek, P., Borkovec, J., Svindrych, Z. & Hagen, G. M. ThunderSTORM: a comprehensive ImageJ plug-in for PALM and STORM data analysis and super-resolution imaging. *Bioinformatics* 30, 2389–2390 (2014).

75. Huang, B., Wang, W., Bates, M. & Zhuang, X. Three-dimensional super-resolution imaging by stochastic optical reconstruction microscopy. *Science* 319, 810–813 (2008).

76. Chen, K.-C. J., Yang, G. & Kovacevic, J. in *2014 IEEE International Conference on Image Processing (ICIP)* 867–871 (IEEE, 2014).

77. Otsu, N. A threshold selection method from gray-level histograms. *IEEE Trans. Syst. Man Cybern.* 9, 62–66 (1979).

78. Stone, M. B. & Veatch, S. L. Steady-state cross-correlations for live two-colour super-resolution localization data sets. *Nat. Commun.* 6, 7347 (2015).